Energy 363 (2026) 142243

Contents lists available at ScienceDirect

Energy

journal homepage: www.elsevier.com/locate/energy

Thermal performance of an asphalt solar collector coupled to a water-source heat pump for domestic hot water: A system simulation

Lianghan Cong [a,*], Shuaiyi Lu [b], Pan Jiang [b], Lan Liu [c], Xiaoshu Lü [a,d]

[a] Renewable Energy and Built Environment, School of Technology and Innovations, University of Vaasa, P.O. Box 700, FIN-65101, Vaasa, Finland
[b] Construction Engineering College, Jilin University, Changchun, Jilin, 130026, China
[c] School of Management, University of Vaasa, P.O. Box 700, FIN-65101, Vaasa, Finland
[d] Department of Civil Engineering, Aalto University, P.O.Box 12100, FIN-02150, Espoo, Finland

ARTICLE INFO

Keywords:
Asphalt solar collector
Solar-assisted heat pump
Domestic hot water
Urban pavement energy harvesting
High-latitude climate
Model validation

ABSTRACT

Electrification is increasing the use of heat pumps for domestic hot water (DHW), but their performance remains strongly dependent on source temperature. This study evaluates whether an asphalt solar collector (ASC) integrated into a 600 m^2 parking area can provide seasonal source-side preheating for a water-source heat pump in Kaunas, Lithuania (54.9°N). An hourly model was run for 2015–2024 using ERA5 meteorological data and measured DHW demand. Building and vehicle shadows were represented through clipped polygon unions, collector heat transfer and hydraulics through flow-regime-specific correlations, and heat-pump capacity and electricity use through a manufacturer-based EN 14511 performance map that included operating limits, cycling, backup heating, standby demand and hydraulic auxiliaries. Under fixed-flow control, the shaded collector delivered 25.06 kWh m^{-2} yr^{-1} and increased the heat-pump seasonal coefficient of performance from 3.58 to 4.01. After collector pumping was included, the system seasonal performance factor was 3.92 and net electricity use fell by 8.66%. Variable-flow strategies increased gross heat collection by 4.6–4.7%, but reduced net electricity savings to 6.60–7.04% because of higher pumping demand. Across collector areas of 300–900 m^2 and storage volumes of 2.5–10 m^3, the maximum electricity-saving ratio was 9.80%. Meaningful collection occurred mainly from April to October, and neither economic nor carbon payback was achieved within the assumed 25-year service life. The system should therefore be regarded as a seasonal efficiency measure rather than a year-round heat source, with stronger prospects in sunnier, less shaded locations or projects that can realise additional pavement-related benefits.

Nomenclature

Symbol	Definition
A_{asc}	ASC area (m^2)
C_p	specific heat of water (J kg^{-1} K^{-1})
COP	coefficient of performance (–)
ESR	net electricity saving ratio (%).
f_{bldg}, f_{car}	building/vehicle shading fractions (–)
G_{sw}, G_{eff}	incident/effective shortwave irradiance (W m^{-2})
h_{conv}, h_{rad}, h_{ext}	convective, radiative, fluid-side heat-transfer coefficients (W m^{-2} K^{-1}).
J	net thermal-benefit objective of the flow controller, $J = Q - COP \cdot P_{pump}$ (pump power as thermal-equivalent) (W)
$\dot{m}$	module mass flow rate (kg s^{-1})
NTU	number of transfer units (–)
P_{pump}	circulation-pump electrical power (W).
Q	collected heat (Q_{asc} total; Q_{mod} per module; Q_{net} after transport loss) (W or kWh)
R_{cond}, R_{wall}, R_{conv}	asphalt, pipe-wall, internal-convective thermal resistances (m K W^{-1})
s_{pipe}	pipe spacing (m).
T_{surf}, T_{in}, T_{out}, T_{tank}, T_{cw}	pavement-surface, inlet, outlet, buffer-tank, cold-water temperatures (°C)
T_{sink}, T_{source}	condenser/evaporator temperatures (K)
UA_{mod}	module overall heat-transfer coefficient (W K^{-1})
v_{wind}	wind speed (m s^{-1})
z_p	pipe burial depth (m).
α	pavement albedo
ε	pavement emissivity/exchanger effectiveness
C_{dh}	cycling degradation coefficient (–)
η_{pump}, η_{motor}, η_{VFD}	pump, motor, VFD efficiencies

* Corresponding author.
E-mail address: lianghan.cong@uwasa.fi (L. Cong).

https://doi.org/10.1016/j.energy.2026.142243
Received 13 April 2026; Received in revised form 5 August 2026; Accepted 19 August 2026
Available online 27 August 2026

(*continued*)

ρ	fluid density (kg m^{-3})
σ	Stefan–Boltzmann constant
ΔT	temperature lift (K).

1. Introduction

In the context of deep decarbonisation of the global building sector, the electrification of heating and the integration of renewable energy have become key pathways for reducing greenhouse gas emissions [1]. In Europe, building heating and domestic hot water (DHW) account for a substantial share of final energy consumption [2], while many existing supply systems still rely on fossil-fuel-based technologies or carbon-intensive district heating networks [3]. As electricity systems continue to decarbonise, electrically driven heat pumps are increasingly regarded as a key option for replacing conventional heating technologies because they can utilise low-grade ambient heat and significantly reduce both primary energy consumption and carbon emissions [4,5].

However, the efficiency of heat pump systems is highly sensitive to the temperature lift between the evaporator and condenser sides [6–8]. In DHW applications, the supply temperature usually needs to reach 50–60 °C to satisfy hygiene and user comfort requirements, which leads to a relatively large temperature lift and, consequently, a lower coefficient of performance (COP) and higher electricity consumption [9,10]. Therefore, increasing the temperature of the evaporator-side heat source while maintaining reliable DHW supply is an effective strategy for improving the energy performance of heat pump systems.

Solar-assisted heat pump (SAHP) systems have been widely recognised as a promising approach for this purpose [11,12]. By coupling solar thermal collectors to the evaporator side of a heat pump, solar energy can be used to elevate the source-side temperature, reduce the required temperature lift, and improve heat pump COP [13]. Previous studies have extensively investigated the integration of flat-plate collectors, evacuated tube collectors, and photovoltaic/thermal (PV/T) systems with heat pumps [14–16]. More recent developments have further expanded this field to include CO_2 transcritical heat pump systems for DHW production [17], ultra-low-temperature district heating with booster heat pumps [18], and model predictive control strategies for solar-assisted DHW systems [19,20].

Compared with conventional medium- and high-temperature solar collectors, low-temperature unglazed collectors are particularly suitable for coupling with heat pump evaporators because they can operate effectively at relatively low source temperatures and maintain longer annual operating periods [21]. In addition, such collectors can be integrated into building envelopes or urban infrastructure surfaces, thereby reducing land-use requirements and avoiding competition for limited rooftop area.

Among potential urban heat-harvesting surfaces, asphalt pavements are of particular interest because they are widespread, highly solar absorptive, and characterised by considerable thermal inertia. By embedding heat-exchange pipes within the pavement structure, asphalt solar collectors (ASCs) can recover solar heat absorbed by the pavement and transfer it to a circulating fluid. This low-temperature heat can then be used as an auxiliary heat source for heat pump systems. In addition to energy recovery, ASC systems may provide further co-benefits, such as reducing pavement surface temperature, mitigating the urban heat island effect, and slowing asphalt thermal ageing [22–25].

Previous studies have investigated the thermal behaviour of ASC systems through both experiments and numerical simulations, showing that their performance is strongly influenced by design and operating parameters such as pipe spacing, burial depth, flow rate, and pavement albedo [25,26]. However, in high-latitude cold climates, solar radiation is relatively weak and exhibits pronounced seasonal variability. Under such conditions, ASC systems generally need to be combined with thermal storage and heat pumps to deliver meaningful annual energy benefits [27]. Despite this potential, the application of ASCs as evaporator-side heat sources for DHW heat pump systems remains insufficiently studied, particularly in high-latitude urban environments.

Three major research gaps can be identified in the existing literature. First, most previous studies on pavement solar collection have primarily focused on maximising thermal yield, whereas relatively few have assessed overall electricity-saving performance by jointly considering collected heat, circulation pump electricity consumption, and the resulting improvement in heat pump COP [28]. This issue is particularly important because the auxiliary electricity demand of the circulation pump may materially affect the net benefit of ASC systems, especially in small- and medium-scale applications. Second, in high-latitude urban environments, low solar elevation angles can cause substantial and highly dynamic shading from surrounding buildings and parked vehicles. If such effects are not explicitly represented, the available solar irradiance on the pavement may be systematically overestimated, leading to overly optimistic predictions of system performance. Third, many previous studies have relied on short-term experiments or single-year simulations based on typical meteorological year data, whereas long-term evaluations based on multi-year meteorological records remain limited.

To address these gaps, this study investigates the DHW system of the B92 residential building in Kaunas, Lithuania (54.9°N), where a 600 m^2 parking-lot ASC is coupled with a water-source heat pump and a low-temperature buffer tank. Hourly simulations were conducted over a ten-year period (2015–2024) using ERA5 reanalysis data. Within this framework, one fixed-flow control strategy and two variable-flow control strategies were systematically compared, while the effects of building shading and vehicle shading were explicitly incorporated into the model.

This study evaluates ASC–heat-pump performance using net ESR rather than gross heat yield, thereby accounting explicitly for collector output, circulation-pump electricity, control strategy, and heat-pump performance. The analysis shows that variable-flow control can increase heat collection while reducing net electricity savings when hydraulic losses and drive efficiency are included. The framework combines ten years of reanalysis meteorology with measured demand data, hourly building and vehicle shading, and comparisons of the collector sub-model with three published installations spanning 38–63°N. Component-level evaluation, uncertainty analysis, design optimisation, and economic and life-cycle assessments are then used to define the feasibility and limitations of the proposed system.

2. Materials and methods

Fig. 1 and the following sequence summarise the coupled modelling framework. At each hourly time step, the model (i) calculates effective pavement irradiance from ERA5 radiation after building and vehicle shading; (ii) solves pavement surface temperature using a linearised Hottel–Whillier energy balance; (iii) calculates module heat collection with an ε–NTU heat-exchanger model under the selected control strategy; (iv) updates buffer-tank temperature from its energy balance; and (v) evaluates heat-pump COP and electricity demand against the DHW load. The sub-models are coupled sequentially through the buffer-tank state, and net ESR is the primary annual output. The framework was implemented in Python using NumPy and Pandas for numerical calculations and openpyxl to process the measured demand input. The governing equations, parameter values, control logic, and workflow are fully specified in Section 2, Appendices A1–A3, and Supplementary Table S1, providing a reproducible computational procedure without relying on code availability. The DHW input is derived from measured district-heating substation records for the B92 building, as described in Section 3.1.

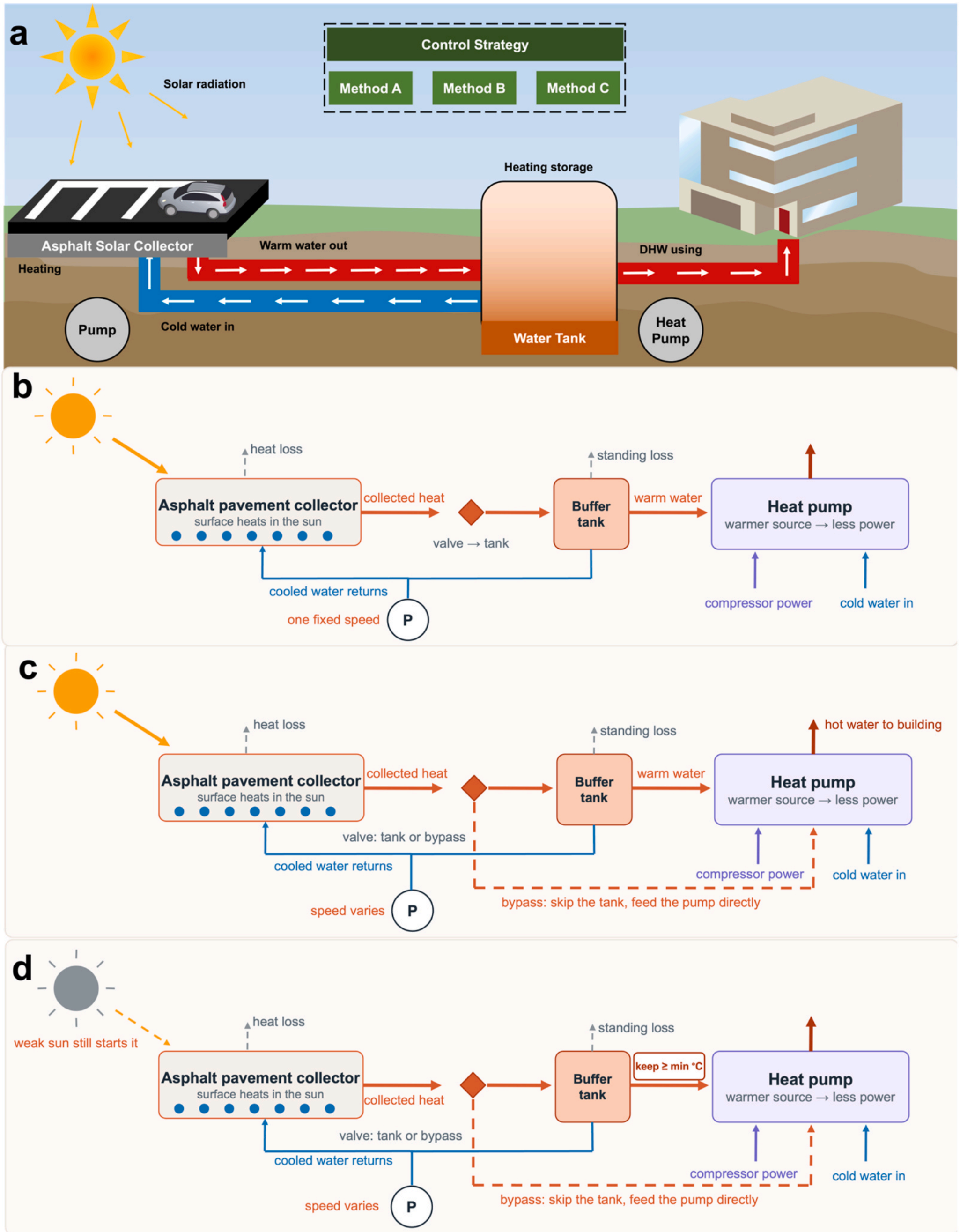

Fig. 1. System schematic of the parking-lot asphalt solar collector coupled to a low-temperature buffer tank and a water-source heat pump for domestic hot water production.

2.1. Study location and system overview

This study was conducted in Kaunas, Lithuania (54.9°N, 23.9°E). Kaunas has a temperate continental climate, with an annual mean air temperature of approximately 9 °C and an annual global horizontal irradiance (GHI) of approximately 1050 kWh m^{-2} [29,30]. Compared with southern European regions, summer pavement temperatures are relatively moderate, with typical daytime values of 22–34 °C. Fig. 2 presents the satellite image and site photograph of the study area. These climatic and site characteristics make Kaunas a representative case for evaluating the feasibility of coupled ASC–heat pump systems under high-latitude cold-climate conditions.

The investigated system is the DHW supply system of the B92 residential building. Adjacent to the building is a parking lot with an area of approximately 600 m^2, beneath which collector pipes are embedded in the asphalt pavement. The overall system configuration is illustrated in Fig. 1. The ASC absorbs solar heat from the pavement surface and transfers it to a low-temperature buffer tank through insulated transport pipes. A water-source heat pump then uses the buffer tank as the evaporator-side heat source and upgrades the collected heat to a DHW supply temperature of 50 °C. By increasing the buffer tank temperature and reducing the required temperature lift, the ASC enhances heat pump COP and reduces overall electricity consumption.

It should be emphasised that the ASC operates exclusively in solar collection mode. During periods without sufficient solar radiation, such as nighttime and winter conditions, no heat is extracted from the pavement. Ground-source heat extraction is not considered because the shallow burial depth (5 cm) is insufficient for effective ground-coupled

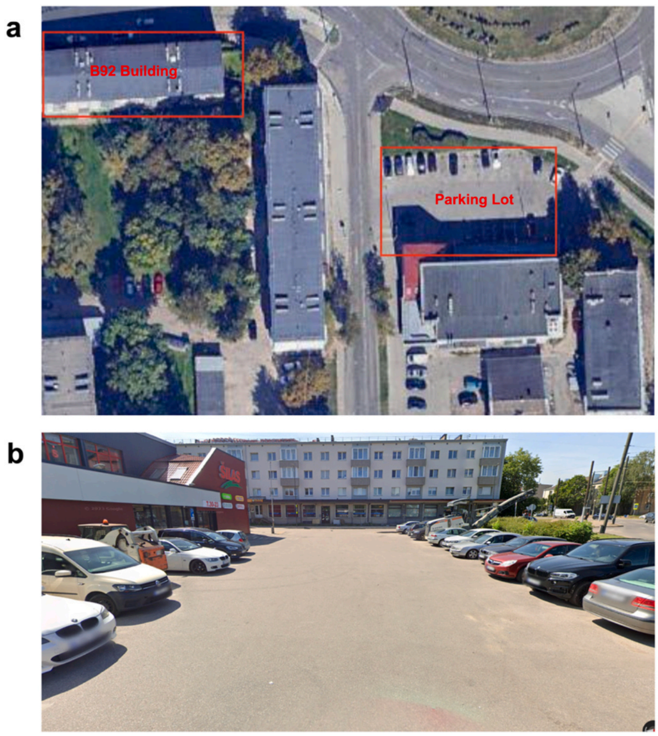

Fig. 2. (a) Satellite view of the building and parking lot; (b) on-site view of the parking lot (source: Google Maps).

operation, and excessive heat extraction from shallow pavement layers could increase the risk of frost heave and structural deterioration. When the buffer tank temperature falls below the cold water temperature, the heat pump draws heat directly from the cold water supply.

The main design parameters of the system are summarised in Table 1.

2.2. Meteorological data

Hourly ERA5 reanalysis data from the European Centre for Medium-Range Weather Forecasts (ECMWF) were used as meteorological inputs

Table 1
Main design parameters of the system.

Parameter	Value	Unit	Description
ASC area	600	m^2	Parking lot area
Pipe spacing	0.20	m	Centre-to-centre
Pipe inner/outer diameter	20/24	mm	PEX pipe
Pipe burial depth	50	mm	Below pavement surface
Flow rate (Method A)	0.05	kg s^{-1} $module^{-1}$	Fixed-flow control
Flow rate range (Methods B/C)	0.008–0.100	kg s^{-1} $module^{-1}$	Variable-flow control
Buffer tank volume	5000	L	Low-temperature buffer
Upper tank temperature limit	40	°C	Storage-control limit; heat-pump source limited to 30 °C
DHW supply temperature	50	°C	Condenser-side outlet
Heat-pump performance model	Daikin EWSAH06D9W	—	Six EN 14511 nodes; −10 to 30 °C source operating envelope
Asphalt thermal conductivity	1.0	W m^{-1} K^{-1}	Dense asphalt concrete
Pavement albedo	0.10	—	Black asphalt surface
Pavement emissivity	0.95	—	Long-wave emissivity

for the period from 1 January 2015 to 31 December 2024, corresponding to 87,672 hourly records. The extracted variables included 2 m air temperature, 10 m wind components, surface downward shortwave radiation, and surface downward longwave radiation. In ERA5, radiation variables are stored as accumulated quantities. Therefore, hourly mean irradiance was obtained by differencing consecutive accumulated values and dividing by 3600 s, with negative values at reset points set to zero.

In ERA5, radiation data are stored as accumulated values from the forecast start time and are reset to zero at 01:00 UTC each day. The hourly mean irradiance was obtained by differencing two adjacent accumulated values and dividing by 3600 s:

$$G_{sw(t)} = \frac{max[ssrd(t) - ssrd(t-1), 0]}{3600} \tag{1}$$

Over the ten-year period, annual GHI ranged from 975 to 1104 kWh m^{-2}, which is consistent with measured data for Kaunas within ±5% [29]. The ten-year meteorological dataset is presented in Fig. 3, including the monthly air temperature range (Fig. 3a), global horizontal irradiance (Fig. 3b), and wind speed (Fig. 3c).

The wind speed at ground level was calculated from the $u10$ and $v10$ components:

$$v_{wind} = \sqrt{(u10^2 + v10^2)} \tag{2}$$

2.3. Solar position and shading model

2.3.1. Solar position

The solar altitude and azimuth angles were calculated hourly using the Spencer equations [31]. The deviation from the NREL solar position algorithm (SPA) is less than 0.5°. The day angle B (rad) is defined as:

$$B = \frac{2\pi(d_n - 1)}{365} \tag{3}$$

The equation of time E (min) is given by:

$$E = 229.18(7.5e - 5 + 1.8 - 2sinB - 1.4615e - 2\cos 2B - 0.04089 \sin 2B) \tag{4}$$

The solar declination and hour angle were then derived from the solar time. Finally, the solar altitude alt (°) and azimuth az (°; clockwise from north) were determined. When, the sun is below the horizon and irradiance was set to zero.

2.3.2. Building shading model

The parking lot is represented as a 30 m × 20 m horizontal polygon. The adjacent building is represented by its measured façade width, height, orientation, and clear distance from the lot. At each hour, the upper building vertices are projected onto the pavement along the solar vector. The convex hull of the footprint and projected vertices defines the building-shadow polygon, which is clipped to the parking-lot boundary.

$$S = \frac{H}{tan(alt)} \tag{5}$$

This vector projection retains the effects of solar altitude, solar azimuth, façade orientation, edge clipping, and finite building width.

$$P = max(S \cdot cos\,\theta_{az} - D_{clear}, 0) \tag{6}$$

The hourly building-shaded fraction is the area of the clipped shadow polygon divided by the parking-lot area.

$$f_{bldg} = min\left(\frac{P}{L_{depth}}, 1\right) \tag{7}$$

2.3.3. Vehicle shading model

The parking lot contains 20 parking spaces. Representative vehicle

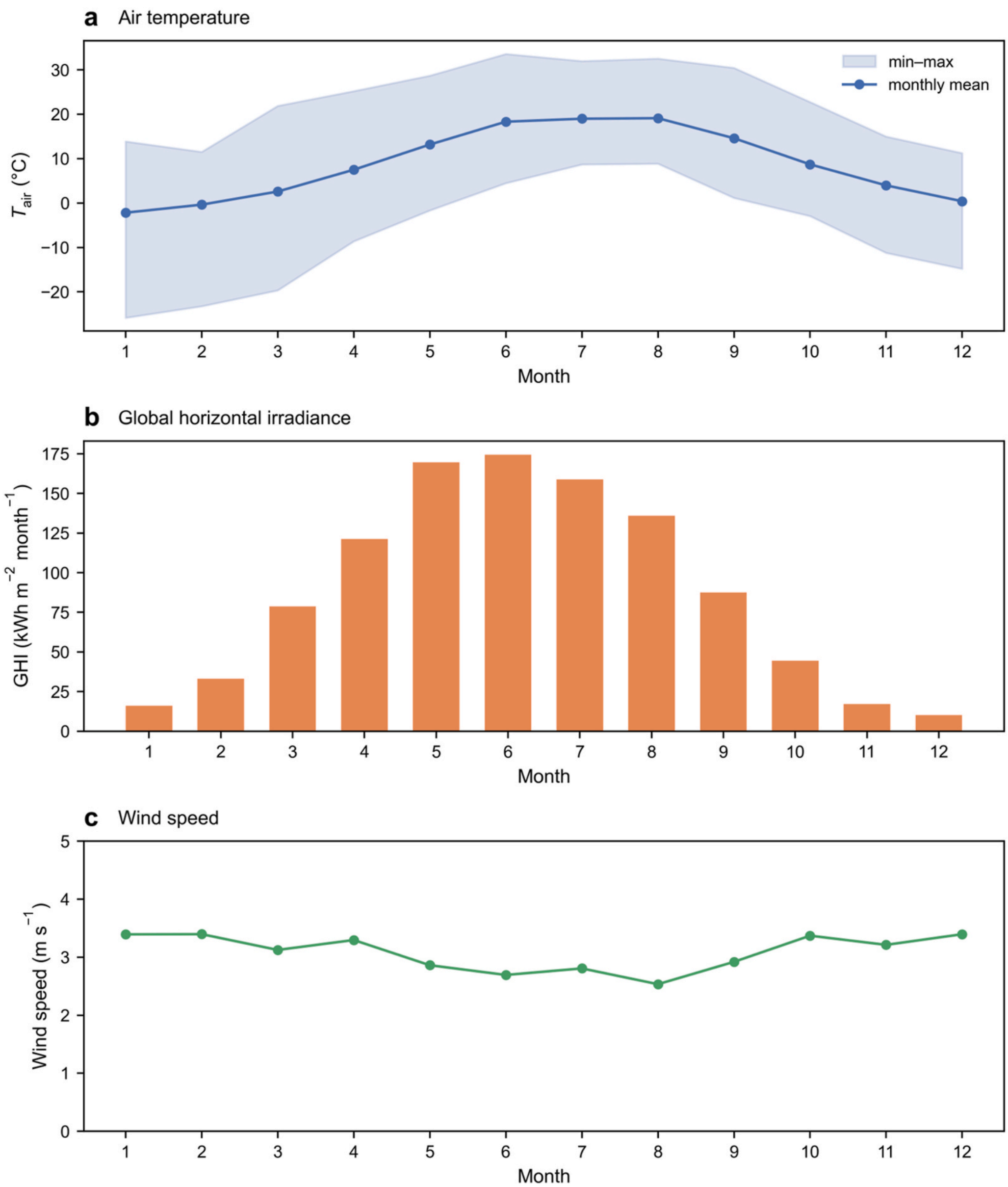

Fig. 3. Ten-year meteorological data for Kaunas (2015–2024): (a) monthly air temperature range, (b) monthly global horizontal irradiance, (c) monthly mean wind speed.

dimensions were set to 1.5 m in height, 4.5 m in length, and 1.8 m in width, consistent with average dimensions of the European M1 passenger vehicle category reported by the European Automobile Manufacturers' Association (ACEA) [32]. The parking occupancy rate was assumed to be 70% during supermarket business hours (08:00–20:00 local time) and 10% during the remaining hours, based on typical commercial parking utilisation rates reported in the *ITE Parking Generation Manual* [33].

Each occupied space is represented as an oriented 4.5 m × 1.8 m × 1.5 m rectangular prism. For each sun position, the four roof vertices are projected onto the pavement; the convex hull of the vehicle footprint and its projected roof forms the shadow polygon. All vehicle polygons are clipped to the lot and combined by geometric union, so overlap is counted once. The union is then combined with the building shadow before the shaded fraction is evaluated.

$$A_{car} = l_{car} \cdot h_{car}\ tan(alt) \cdot cos\ \theta_{az} \tag{8}$$

$$f_{car} = min\left(\frac{N_{occ} \cdot A_{car}}{A_{total}}, 1\right) \tag{9}$$

Vehicle occupancy is imposed hourly using the stated business-hour schedule. The polygon algorithm was checked against the closed-form isolated-prism projection and independently against a ray–box intersection mask. The maximum isolated-area error was 0.283%; the polygon and ray-casting masks agreed at the validation-grid resolution (maximum shaded-fraction error 0 and intersection-over-union 1.0).

2.3.4. *Effective irradiance*

Effective pavement irradiance is calculated from the incident shortwave irradiance multiplied by one minus the area fraction of the combined building–vehicle shadow union.

$$G_{eff} = G_{sw} \cdot \left(1 - f_{bldg}\right) \cdot (1 - f_{car}) \tag{10}$$

2.4. ASC heat transfer model

2.4.1. Series thermal resistance

The heat transfer path in the ASC can be simplified as pavement absorption, heat conduction through asphalt, heat conduction through the pipe wall, internal convection inside the pipe, and heat transfer to the circulating fluid. These three thermal resistances (K m W^{-1}) were calculated per unit pipe length.

The conductive thermal resistance through the asphalt layer was calculated using the buried-cylinder shape factor model [34]. With outer pipe radius $r_o = 0.012$ m and burial depth $z_p = 0.05$ m:

$$R_{cond} = \frac{ln\left(2\frac{z_p}{r_o}\right)}{(2\pi \cdot k_{asph})} \tag{11}$$

The pipe wall conductive resistance for the PEX pipe was calculated as:

$$R_{wall} = \frac{ln\left(\frac{r_o}{r_i}\right)}{(2\pi \cdot k_{pipe})} \tag{12}$$

where $k_{pipe} = 4\ 5 W\, m^{-1}\, K^{-1}$.

The internal convective resistance was determined from the convective heat h_i, which was calculated using the Gnielinski correlation for $Re \geq 2300$.

$$Nu = \frac{\left(\frac{f}{8}\right)\cdot(Re - 1000)Pr}{\left[1 + 12.7\sqrt{\frac{f}{8}}\cdot\left(Pr^{\frac{2}{3}} - 1\right)\right]} \tag{13}$$

where f is the Petukhov friction factor, and is the Prandtl number of water at 20 °C.

$$G_{eff} = G_{sw}\cdot\left(1 - f_{bldg}\right)\cdot(1 - f_{car}) \tag{14}$$

$$R_{conv} = \frac{1}{(2\pi \cdot r_i \cdot h_i)} \tag{15}$$

The total thermal resistance and the overall heat transfer coefficient of one module, UA_{mod}, W K^{-1} are given by:

$$h_i = Nu\cdot\frac{k_f}{D_i} \tag{16}$$

$$R_{total} = R_{cond} + R_{wall} + R_{conv} \tag{17}$$

$$UA_{mod} = \frac{L_{pipe}}{R_{total}} \tag{18}$$

where $L_{pipe} = \frac{A_{mod}}{s_{pipe}}$ is the total pipe length per module (m), and s_{pipe} is the pipe spacing.

2.4.2. Heat transfer effectiveness

From heat exchanger theory, the ε-NTU method covers a range of heat capacity ratio configurations. When one side has an effectively infinite thermal capacity, i.e. $C_r = \frac{C_{min}}{C_{max}} \rightarrow 0$, the heat transfer effectiveness reduces to Ref. [35]. Details can be found in Appendix A1.

2.5. Pavement surface temperature model

The pavement surface temperature is a key driving variable for ASC heat collection. In this study, the Hottel–Whillier linearised heat balance equation was used to describe the steady-state energy balance of the pavement surface [36]. The pavement is subjected to solar gain, radiative heat loss, convective heat loss, and heat conduction to the circulating fluid through the embedded pipes. Details are provided in Appendix A2.

In the present model, summer peak pavement temperatures range from 38 to 48 °C for air temperatures of 25–33 °C, while winter minimum pavement temperatures are approximately −20 °C at air temperatures of −26 °C (Fig. 4a). The scatter plot of daytime T_{surf} versus T_{air} (Fig. 4b) also confirms the expected nonlinear relationship driven by solar radiation. Overall, these values are consistent with the reported Lithuanian field measurements within the expected uncertainty range of energy-balance pavement temperature models (±3 °C according to Solaimanian and Kennedy [37]).

2.6. Cold water temperature model

The cold water temperature is one of the key parameters affecting heat pump performance. This study adopted the linear empirical model proposed by Morkunaite et al. [38], which expresses the cold water temperature T_{cw} (°C) as a linear function of the 24 h moving-average outdoor air temperature $\theta_{(out,24h)}$ (°C):

$$\theta_{cw} = 0.2667 \times \theta_{(out,24h)} + 9.3333 \tag{19}$$

where $\theta_{(out,24h)}$ is the 24 h moving average of outdoor air temperature.

To satisfy physical constraints related to freezing protection and water supply conditions, the cold water temperature was limited to the following range:

$$\theta_{cw} = max(4, min(16, \theta_{cw})) \tag{20}$$

The use of a 24 h moving average rather than instantaneous air temperature has a clear physical basis. First, it removes diurnal fluctuations and reflects the daily thermal inertia of the soil around buried water pipes. Second, the linear slope of 0.2667, approximately equal to 1/3.75, represents the attenuation of seasonal temperature amplitude at a burial depth of about 2 m, which is consistent with the analytical attenuation factor in the Kasuda and Achenbach model [39]. Third, the intercept of 9.3333 °C corresponds to the annual mean underground temperature in Kaunas and agrees with measured local ground temperatures of about 9–10 °C.

2.7. Heat loss in the transport pipe

The heat collection fluid from the ASC is transported to the indoor buffer tank through a 25 m insulated buried pipe. The heat loss in the pipe was calculated according to EN ISO 15698 using a linear heat transfer coefficient representative of a DN25 pre-insulated pipe:

$$Q_{pipe} = U\cdot L\cdot max\left(T_{fluid} - T_{ground}, 0\right) \tag{21}$$

where T_{fluid} is the average fluid temperature (°C).

The pipe heat loss was capped at 30% of the ASC heat output as a physical upper bound, and it was counted only when the pump was operating $Q_{asc} > 0$. Under typical conditions, pipe heat loss accounted for 2–8% of ASC heat output and had only a minor effect on the annual energy balance.

2.8. Manufacturer-based water-source heat-pump model

2.8.1. Performance-map interpolation and operating constraints

Heat-pump capacity and compressor electricity were calculated from the manufacturer performance map for the Daikin Altherma 3 WS EWSAH06D9W, selected because its nominal capacity is consistent with the simulated DHW load (mean 3.48 kW; maximum 6.85 kW).

The EN 14511:2018 catalogue provides heating capacity and electric input at the six source/load test points W10/W35, W10/W55, W20/W35, W20/W55, W25/W35, and W25/W55. Capacity and input are bilinearly interpolated at the hourly source temperature and a 50 °C load-side leaving-water temperature.

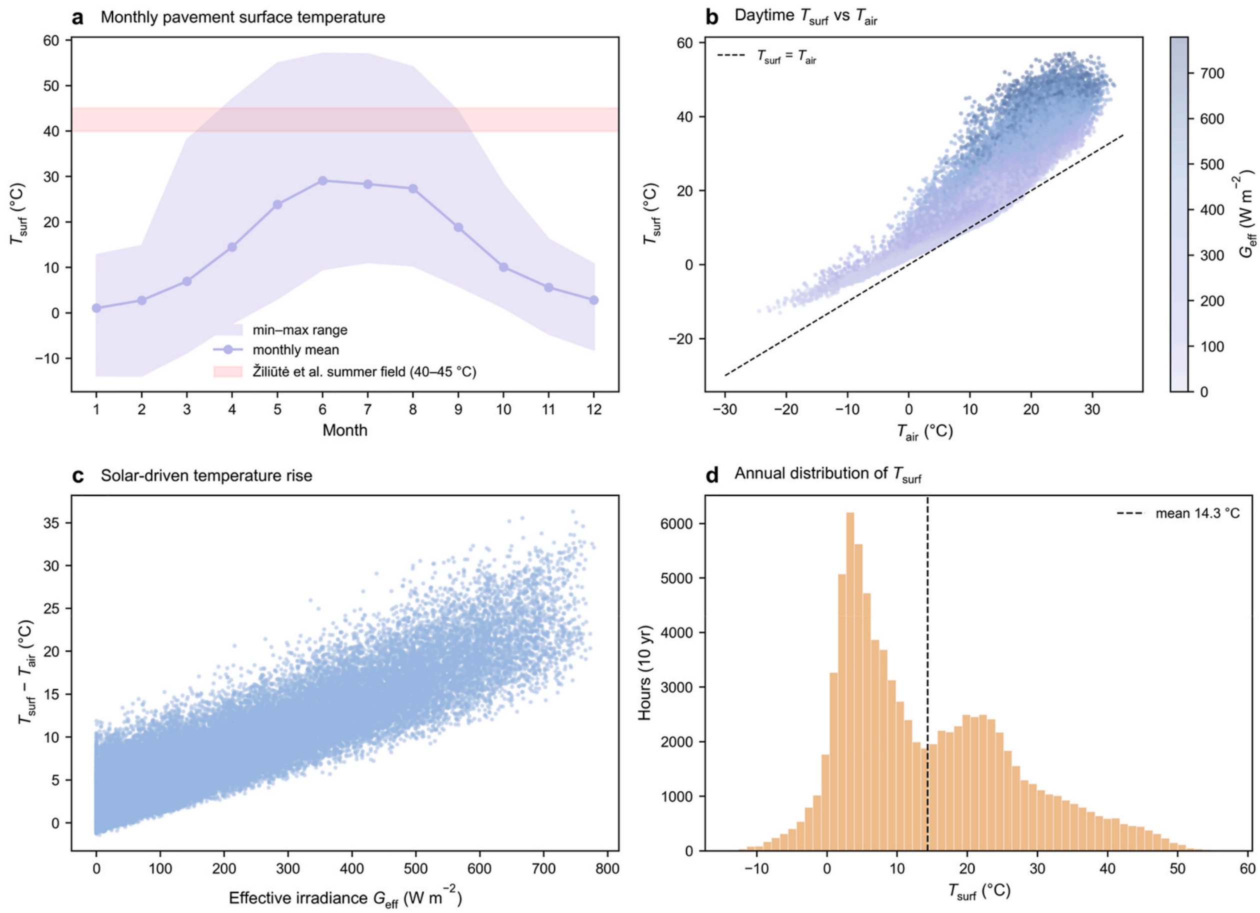

Fig. 4. Pavement surface temperature model validation. (a) Monthly pavement surface temperature (min–mean–max band) with the Žiliūtė et al. summer field range (40–45 °C); (b) daytime T_{surf} vs T_{air} coloured by effective irradiance; (c) solar-driven temperature rise ($T_{surf} - T_{air}$) vs irradiance; (d) annual distribution of T_{surf}.

Bilinear interpolation is used within the measured 10–25 °C source and 35–55 °C load-temperature rectangle. Outside the measured source range, adjacent edge trends are extended only within the published −10 to 30 °C source-water operating envelope. The load temperature is not extended beyond the measured range. A boundary-clamped case is reported as a conservative check.

The published modulation range is 0.85–7.98 kW. The hourly calculation is limited to the more conservative interpolated nominal capacity; unmet load is supplied by electric backup heat with COP = 1. Below the minimum modulation capacity, cycling degradation is evaluated using the default coefficient $C_{dh} = 0.9$. Source- and load-loop hydraulic auxiliaries, a 10 W standby demand, and ASC circulation-

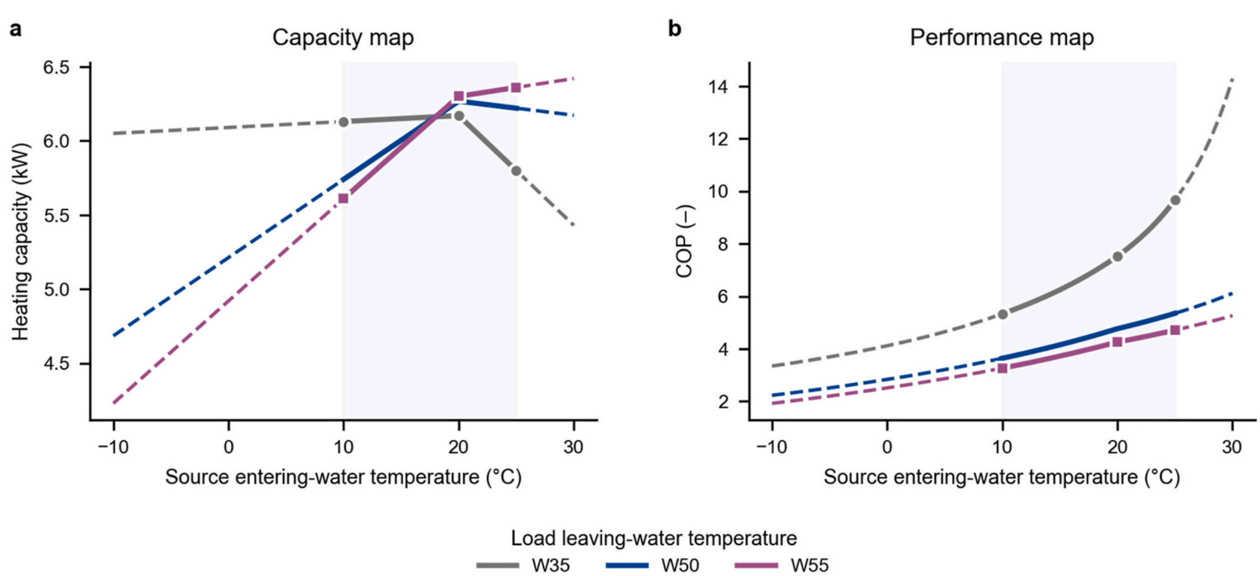

Fig. 5. Manufacturer performance data and bounded bilinear interpolation for the Daikin EWSAH06D9W at 35–55 °C load-side leaving-water temperature.

pump electricity are included explicitly.

2.8.2. SCOP and system SPF definitions

Heat-pump seasonal coefficient of performance (SCOP) is defined as annual DHW heat delivered divided by annual heat-pump electricity, including compressor, internal hydraulic auxiliaries, standby demand, and backup heat. System seasonal performance factor (SPF_{sys}) uses the same delivered heat but additionally includes ASC circulation-pump electricity in the denominator. These energy-weighted ratios are used throughout the analysis instead of an arithmetic mean of hourly COP.

At the six manufacturer nodes, the interpolation reproduces capacity and input exactly. A leave-one-source-level check at 20 °C gave capacity and input RMSE values of 0.228 kW and 0.026 kW, respectively. The resulting seasonal indicators are therefore calculated from an auditable manufacturer map rather than a fitted Carnot-efficiency curve. The manufacturer performance data and the bounded bilinear interpolation are shown in Fig. 5.

The baseline and ASC-assisted cases use the same heat-pump model, DHW load, 50 °C delivery temperature, and auxiliary assumptions. They differ only in the incremental ASC subsystem: collector pipes, transport loop, low-temperature buffer tank, circulation pump, and controls.

$$\eta_{HP}(\Delta T) = \eta_{HP,ref} \cdot [1 - 0.003 \cdot max(\Delta T - 25, 0)] \tag{24}$$

2.9. Low-temperature buffer tank model

The 5000 L tank is an incremental ASC-specific low-temperature source reservoir. A fully mixed hourly energy balance is used, with the tank temperature bounded below by the cold-water temperature and above by 40 °C [40]. The heat-pump performance used for performance calculations is limited to 30 °C; above the measured 25 °C source-temperature boundary, the adjacent edge trends are extended only within he manufacturer-published operating envelope.

$$MC_p \frac{dT_{tank}}{dt} = Q_{net,ASC} - Q_{extracted,HP} - Q_{stand} \tag{25}$$

Tank stratification is not credited in the base case. Its possible effect is treated as model-form uncertainty rather than asserted to make the base estimate conservative [41].

2.10. Heat collection control strategies

To evaluate the influence of control strategy on heat collection and net electricity savings, three pump control methods were designed and compared. Table 2 shows a comparison of the three methods; details can be found in Appendix A3.

The circulation-pump electricity is modelled explicitly. The pressure rise across one module, Δp, is the sum of Darcy–Weisbach pipe friction

Table 2
Comparison of the three control strategies.

Feature	Method A	Method B	Method C
Flow rate	Constant 0.05 kg s^{-1}	Dynamically optimized	Constrained optimisation
Objective	N/A	Maximise gross collected heat Q (pump power not penalised)	Maximise net benefit $J = Q - \mathrm{COP} \cdot P_{pump}$, with $m \geq 0.02$ kg s^{-1} floor
Minimum irradiance threshold	50 W m^{-2}	50 W m^{-2}	20 W m^{-2}
Mode 2 (bypass)	No	Yes	Yes
Additional hardware cost	Baseline (lowest)	Variable-speed pump + controller	Variable-speed pump + controller + three-way valve
Intended application	Reference case	Naïve maximum-harvest benchmark	Net-aware (electricity-saving) optimisation

Table 3
Scenario, uncertainty, and design-variable settings.

Parameter	Baseline value	Range	Physical meaning
Daytime vehicle occupancy	70%	30–90%	Scenario-based uncertain input
Heat-pump map treatment	Full envelope	Measured bound/ upper/full envelope	Performance-map treatment
ASC pump input	172 W	150–280 W	Equipment and hydraulic sensitivity
ASC area/tank volume	600 m^2/5 m^3	300–900 m^2/2.5–10 m^3	Controllable design variables

and a fixed minor/static allowance, $\Delta p = f \cdot (L_{pipe}/D_i) \cdot ½ \cdot \rho \cdot v^2 + 40$ kPa, with the friction factor f from the Blasius relation; the pump electrical power serving n modules is then $P_{pump} = (\dot{m} \cdot n \cdot \Delta p)/(\rho \cdot \eta_{pump} \cdot \eta_{motor} \cdot \eta_{VFD})$, where $\eta_{pump} = 0.60–0.80$ (rising with flow), $\eta_{motor} = 0.90$ and $\eta_{VFD} = 0.95$ ($\eta_{VFD} = 1$ for the fixed-flow Method A, which needs no drive). Because $v \propto \dot{m}$ and $\Delta p_{friction} \propto v^2$, pump power rises steeply (approximately cubically) with flow, which is the physical origin of the net penalty of variable-flow control reported in Section 3.2. A per-method hydraulic breakdown (mean/peak flow, Reynolds regime, efficiencies and annual pump energy) is given in the Supplementary Material.

2.11. Sensitivity analysis

Sensitivity analyses were organised by evidence type. Scenario and uncertain inputs included daytime vehicle occupancy (30–90%), heat-pump map treatment, ASC pump selection (150–280 W), and a ±5% pavement-model heat-output discrepancy. Controllable design variables comprised ASC area (300–900 m^2) and buffer-tank volume (2.5–10 m^3). All cases used ten-year meteorology, and the baseline values and tested ranges are summarised Table 3.

3. Results and discussion

All results use the measured B92 DHW service of 30.5 MWh yr^{-1}, ten-year Kaunas meteorology, and polygon-union shading. The 70% daytime vehicle-occupancy reference reduces annual incident irradiance by 35.4%; occupancy scenarios from 30% to 90% are reported separately.

3.1. Model validation

The DHW demand used in the simulation was derived from measured data collected at the district heating substation of the B92 building over the period from May 2018 to September 2021, comprising approximately 27,700 hourly records. The measured data included supply temperature (T_{IN}), return temperature (T_{OUT}), flow rate, and thermal power. The mean hourly thermal power was 3.48 kWh, corresponding to an annual DHW demand of approximately 30,500 kWh yr^{-1}. The measured monthly and hourly demand profiles were used as normalised temporal shapes and scaled to this annual total, thereby preserving the realistic temporal characteristics of the building while extending the demand series to the full ten-year simulation period. The measured DHW profile is presented in the Supplementary Material (Section S5).

The model comprises two coupled sub-models: the Hottel–Whillier linearised surface energy balance for pavement surface temperature T_{surf}, and the ε–NTU effectiveness formulation for pipe-fluid heat exchange. Validation proceeds in two steps.

First, analytical self-consistency is verified by substituting the baseline and sensitivity-analysis operating points into $\varepsilon = 1 - \exp(-NTU)$ and confirming that the implementation returns zero numerical deviation from the closed-form solution.

Second, quantitative cross-validation is performed by applying the ASC collector sub-model to three published field installations, which is shown in Section 3.8.

The framework was evaluated at component level. The pavement surface-temperature calculation remained within ±3 °C of published Lithuanian observations. The heat-pump interpolation reproduced all six manufacturer nodes exactly; leave-one-source-level capacity and input RMSE values were 0.228 and 0.026 kW. Polygon shadows were verified analytically and by independent ray–box intersection. These checks do not constitute experimental validation of the integrated system.

Cross-validation results are summarised inFig. 6. For the Johnsson [42] site ($s = 50$ mm, $T_{in} \approx 8$ °C), the model predicts 249 kWh m^{-2} yr^{-1} against a measured 245 kWh m^{-2} yr^{-1} (+1.7%). For the Buscemi [43] site ($s = 200$ mm, conductive concrete), the prediction is 358 kWh m^{-2} yr^{-1} against a FEM-validated 320 kWh m^{-2} yr^{-1} (+12%); the over-prediction is attributed to the Jurges correlation overestimating h_{cv} under high-insolation Mediterranean conditions, consistent with the 4% MAPE reported for the Buscemi FEM under comparable boundary conditions. For the Ghalandari [44] site ($s = 150$ mm, $T_{in} = 14$ °C) no annual yield is reported; instead, the model's supply-temperature sensitivity is illustrated in Fig. 6b, which shows the modelled daily collector efficiency falling steeply as the inlet temperature rises from 8 to 20 °C.

The integrated system delivers 25.06 kWh m^{-2} yr^{-1} using the polygon-union shading calculation. The warm buffer return and differential control restrict collection to hours that can improve the heat-pump source condition.

The supply-temperature mechanism is independently corroborated by Ghalandari et al. [44], who showed experimentally that raising T_{in} from 14 °C to 28 °C reduced heat extraction by a factor of seven — directly confirming the $T_{surf} - T_{in}$ sensitivity inherent in the ε–NTU formulation. The pipe-spacing sensitivity predicted analytically here ($\varepsilon = 0.485$ at 200 mm vs. 0.93 at 50 mm) is corroborated by Buscemi et al. [43], who independently identify spacing reduction as the highest-return design modification in their FEM optimisation.

The quasi-steady pavement representation was treated as model-form uncertainty. A ±5% heat-output multiplier was propagated through the tank and heat-pump calculations without changing meteorology, load, shading, or control logic.

The ±5% heat-output range changed annual heat yield from 24.68 to 25.43 kWh m^{-2} yr^{-1} and ESR from 8.53% to 8.77% (see Fig. 7). The limited ESR response reflects thermal-storage feedback and the bounded heat-pump operating envelope.

3.2. System performance under three control strategies

Table 4 summarises the annual performance of the three control strategies, averaged over the ten-year simulation period.

Method A delivers 25.06 kWh m^{-2} yr^{-1} (15.03 MWh yr^{-1}) and reduces annual system electricity from 8.52 to 7.78 MWh, corresponding to an ESR of 8.66%. Methods B and C increase gross collection by 4.72% and 4.63%, respectively, but their ESR values fall to 6.60% and 7.04% because the extra circulation-pump demand exceeds the marginal heat-pump saving, as summarised in Fig. 8.

This result indicates that greater heat collection does not necessarily translate into greater net system benefit. The inferior performance of variable-flow control arises from three factors. First, the additional heat is collected mainly under marginal operating conditions, such as low irradiance periods, where the associated COP improvement is modest. Second, variable-frequency drive operation introduces additional efficiency losses ($\eta_{VFD} = 0.95$). Third, pump power rises nonlinearly with flow rate because of hydraulic friction, approximately following a cubic relationship with $\dot{m}$. For the present system configuration, the additional complexity and investment associated with variable-flow control are therefore not justified.

The seasonal benefit remains concentrated from April to October. Manufacturer test points span 10–25 °C, while the published source-water operating range extends from −10 to 30 °C. The main seasonal scenario extends only the adjacent edge trends within that operating envelope; the measured-domain boundary case is retained as a conservative lower bound.

During the summer week (Fig. 10a and b), the pavement surface temperature rises to about 50 °C on clear days, the buffer tank warms from roughly 27 °C to the 40 °C upper limit, and the ASC supplies substantial heat during daytime hours. The plotted week is representative rather than extreme: over the full 2015–2024 record, 55% of summer days peak above 40 °C, 32% above 45 °C and 8% above 50 °C, with a 99th-percentile summer daytime surface temperature of ≈51 °C and rare extremes up to 57 °C, so clear-day summer maxima typically fall within a 40–52 °C envelope. During the winter week (Fig. 10c and d), the pavement surface temperature only slightly exceeds the air temperature and stays below the tank temperature, so ASC heat collection is negligible.

3.3. Winter operation and supplementary strategies

The analysis of zero-collection days (Fig. 11) highlights the seasonal limitation of ASC systems at high latitudes. In December and January, essentially all days exhibit zero heat collection from the ASC. From November through February, the ASC contribution is negligible, and the system effectively operates as a conventional heat pump. Meaningful

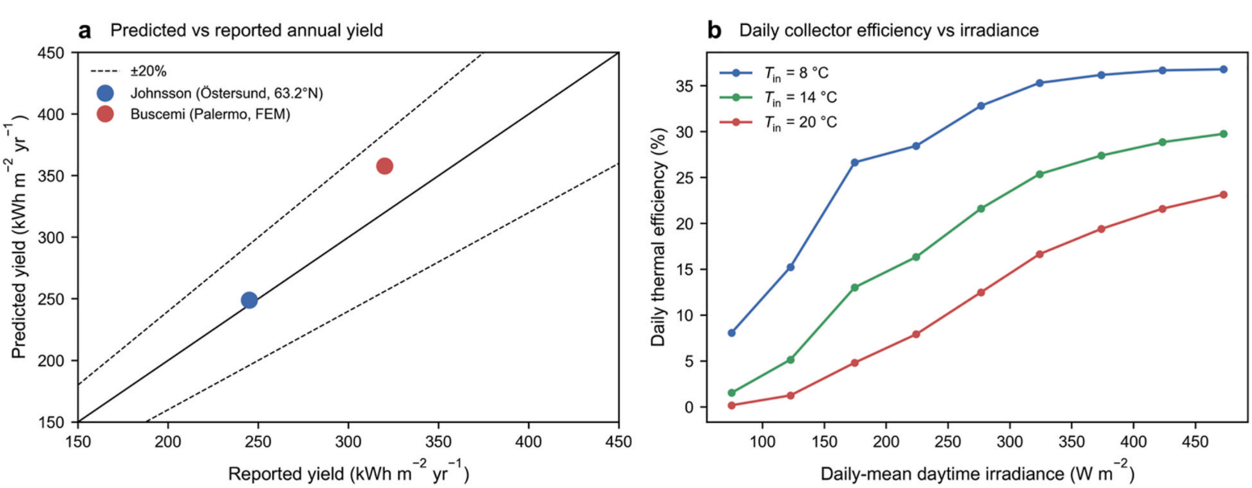

Fig. 6. Cross-validation of the ASC thermal model against published field measurements. (a) Predicted versus reported annual specific heat yield for two sites with measured or FEM-validated annual data; dashed lines indicate ±20% deviation from the 1:1 line. (b) Modelled daily collector efficiency versus daily-mean irradiance for inlet temperatures of 8, 14 and 20 °C under Kaunas conditions, illustrating the supply-temperature sensitivity reported experimentally by Ghalandari et al.

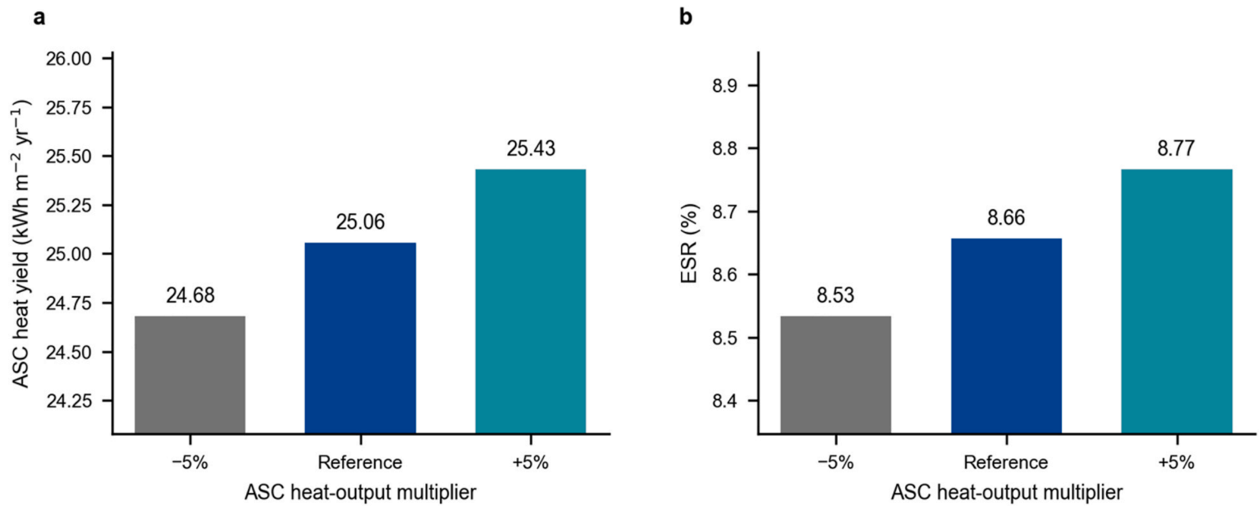

Fig. 7. Propagation of a ±5% pavement-model heat-output discrepancy to (a) annual ASC heat yield and (b) ESR.

Table 4
Annual system performance (10-year average).

Metric	Baseline (no ASC)	Method A	Method B	Method C
ASC heat yield (kWh m^{-2} yr^{-1})	—	25.06	26.24	26.19
ASC annual output (kWh yr^{-1})	—	15,033	15,743	15,716
Net heat to tank (kWh yr^{-1})	—	14,862	15,579	15,551
HP electricity (kWh yr^{-1})	8515	7608	7589	7590
Pump electricity (kWh yr^{-1})	0	170	364	325
Total electricity (kWh yr^{-1})	8515	7778	7953	7915
Heat-pump SCOP	3.58	4.01	4.02	4.02
SCOP improvement (%)	—	+11.9	+12.2	+12.2
Electricity saving ratio (%)	—	8.66	6.60	7.04

ASC operation occurs mainly from April to October, corresponding to an effective operating window of approximately seven months per year.

This winter scarcity is not a shortcoming specific to the ASC concept: it reflects the high-latitude solar resource itself. Any solar-driven technology at this latitude—photovoltaics and roof-mounted solar-thermal collectors alike—delivers only a small fraction of its annual output between November and February (in Kaunas these four months carry less than 8% of the annual GHI; Fig. 3b). The ASC is therefore deliberately not operated for the sake of winter production: the differential controller simply gates collection off, and the investment case rests on the annual net electricity saving, with the winter load served by the heat pump at its baseline COP. It is also worth noting that, in the wider ASC literature, the established winter use of pavement-embedded pipe networks is snow- and ice-melting—a road-service function using stored or auxiliary heat [22]—rather than heat collection; such operation is outside the scope of the present DHW study, but it illustrates that the same buried infrastructure can provide a complementary winter service where required.

It is important to clarify that "winter operation" does not mean that the system stops operating. Although the ASC provides almost no heat, the heat pump continues to meet the full DHW load by extracting heat from the buffer tank, which remains close to the cold-water supply

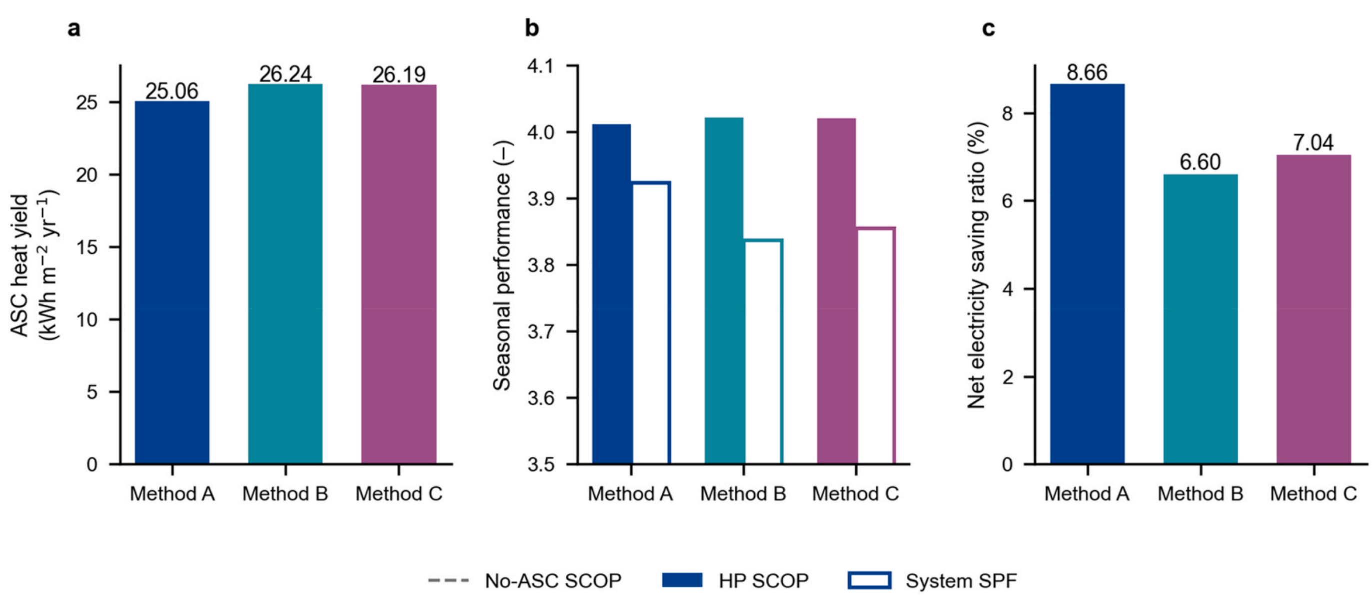

Fig. 8. Control-strategy KPI summary: (a) heat-pump SCOP and system SPF; (b) net electricity-saving ratio. The no-ASC heat-pump SCOP is 3.58.

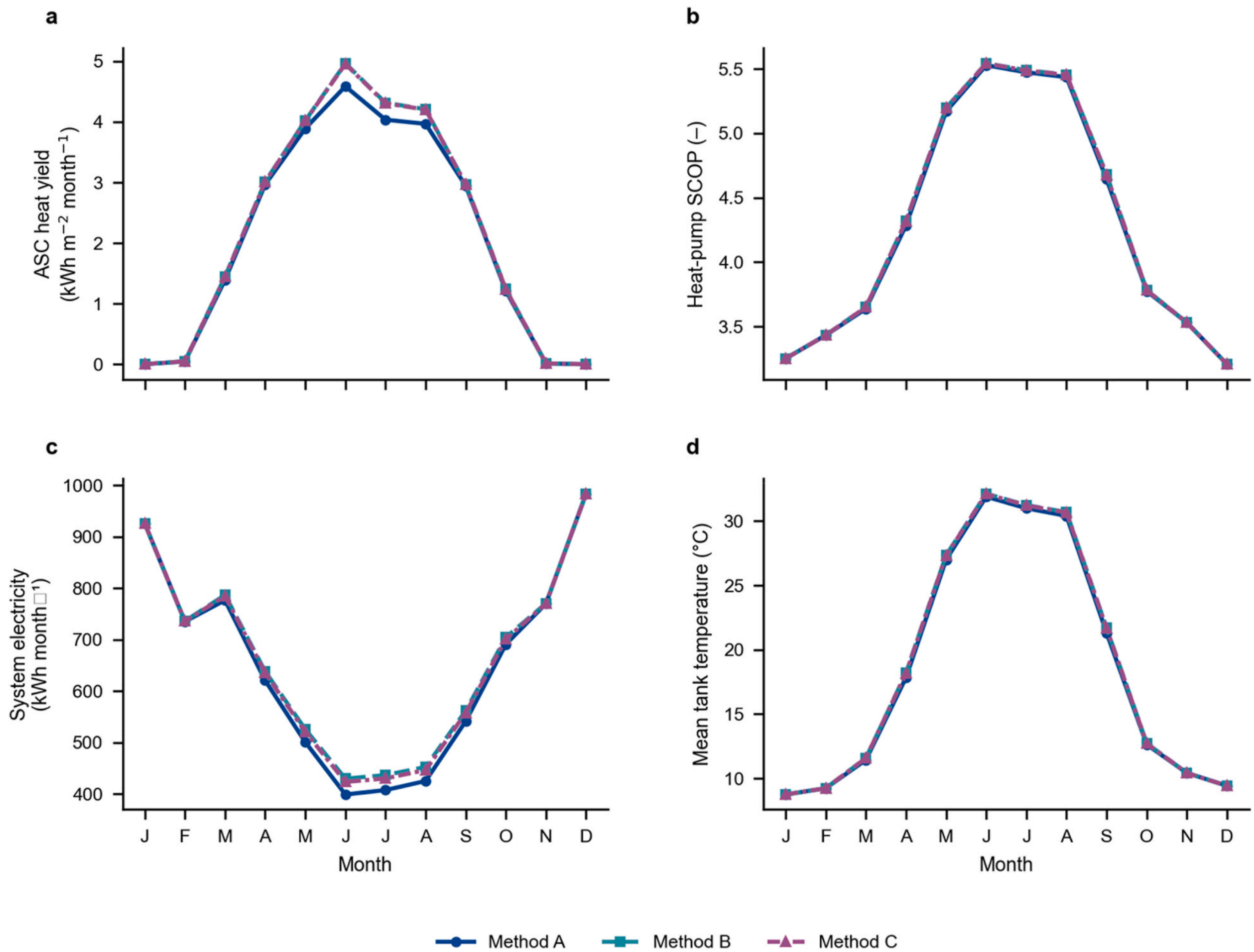

Fig. 9. Monthly system performance (10-year average): (a) ASC heat yield by method, (b) mean COP, (c) electricity consumption, (d) buffer tank temperature range.

temperature of approximately 4–8 °C. Winter therefore presents an efficiency rather than a reliability problem. With a source temperature of about 5 °C and a condenser temperature of 50 °C, the temperature lift is approximately 45 K and the COP falls to its baseline value of about 3.5, equivalent to operation without the ASC. Consequently, the ASC is effectively inactive for around five months each year while the heat pump operates at its lowest efficiency.

Four strategies could address this ASC-free winter period. First, a 50–100 m ground-source heat exchanger could provide a more stable winter heat source while using the same heat pump, although the additional capital cost would be substantial. Second, rooftop photovoltaic generation could offset winter electricity consumption and further reduce operational emissions, despite not increasing thermal collection. Third, seasonal thermal energy storage could transfer summer heat to winter, but the required volume, likely above 100 m^3, would be impractical at the building scale considered. Fourth, reducing the DHW supply temperature from 50 to 45 °C, together with appropriate Legionella control, would lower the winter temperature lift from about 45 to 40 K and increase the winter COP by roughly 10%. Unlike the other options, this measure requires no additional heat-source or storage hardware and provides benefits throughout the year.

This seasonal behaviour explains the apparent mismatch between the December–January DHW demand peak (Fig. S1) and the near-zero ASC output during the same period (Fig. 9). The ASC functions as a COP enhancer rather than a winter heat source. At night and throughout November–February, the heat pump reverts to the cold-water supply as its effective heat source, operates at the baseline COP, and still meets the complete DHW demand. No additional winter strategy is therefore required to ensure reliability.

3.4. Sensitivity and uncertainty analysis

The uncertainty analysis distinguishes uncertain inputs from controllable design variables. Parking occupancy and pavement-model discrepancy are treated as uncertain inputs, whereas collector area, tank volume, pipe spacing, and flow strategy are treated as design variables. Heat-pump curve uncertainty is represented by measured-domain and operating-envelope scenarios, and the principal sensitivity results are summarised in Fig. 12.

No fitted second-law-efficiency parameter is used in the manufacturer-based performance model. SCOP and SPF are recomputed directly from annual delivered heat and electricity for every sensitivity case.

(1) Buffer tank volume.

At 600 m^2, increasing storage from 2.5 to 10 m^3 raises ESR from 7.21% to 9.56%. The gain diminishes as storage volume increases and the source temperature approaches the 30 °C operating limit.

(2) ASC area.

At a 5 m^3 tank volume, changing ASC area from 300 to 900 m^2 increases ESR from 7.92% to 8.65%, with a maximum of 8.69% at 750 m^2. Across the tested 300–900 m^2 and 2.5–10 m^3 design grid, the highest ESR is 9.80% at 900 m^2/10 m^3.

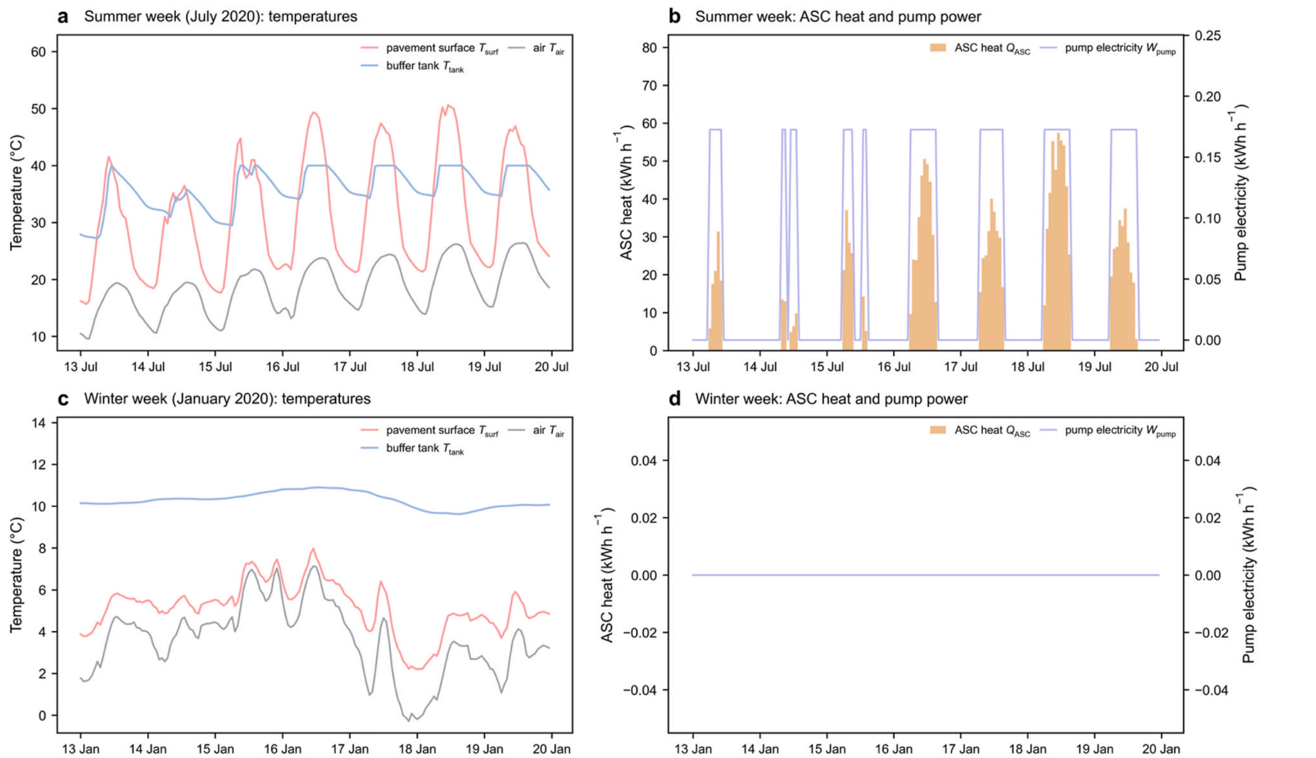

Fig. 10. Typical operating weeks in 2020 (all curves labelled). (a) Summer-week temperatures: pavement surface (up to ~50 °C on clear days), buffer tank (rising to the 40 °C ceiling) and air; (b) summer-week ASC heat output and pump power; (c) winter-week temperatures (pavement only a few °C above air, below the tank); (d) winter-week ASC heat output (≈0).

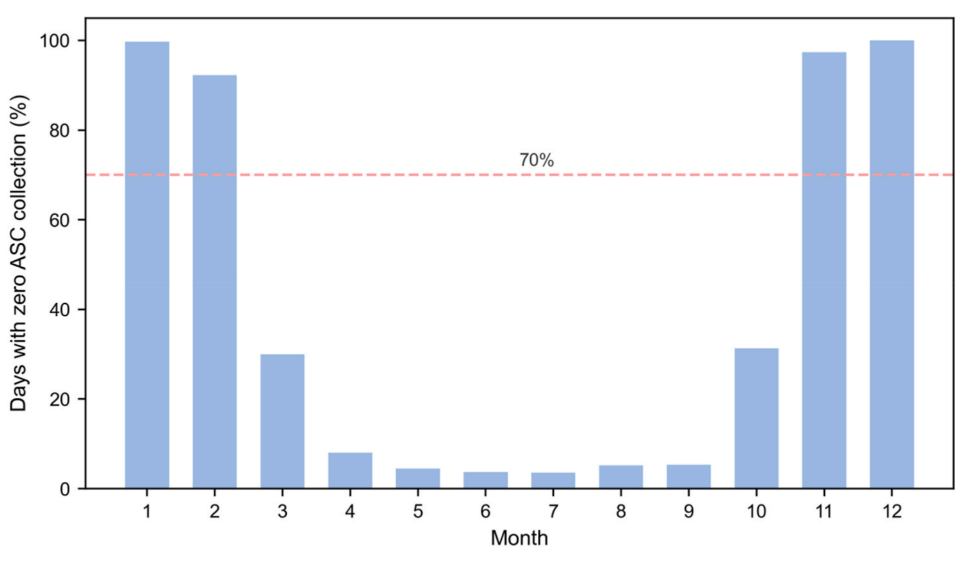

Fig. 11. Seasonal distribution of zero-collection days. From November to February, more than 90% of days have no useful ASC heat output.

(3) Joint area–storage sensitivity.

ESR remains between 6.94% and 9.80% over the tested area–storage domain. Larger storage provides a stronger benefit than increasing collector area at fixed storage volume.

Several secondary assumptions affect the simulation results.

(1) Cold water temperature.

Cold-water temperature is an uncertain boundary input and must be varied jointly in both the no-ASC and ASC-assisted cases. It is therefore not ranked together with controllable design variables in the scenario-range summary.

(2) Transport pipe heat loss.

Transport-pipe heat loss is treated as an uncertain loss coefficient. Its influence is propagated with the same system boundary and annual-energy definitions used for the base case.

(3) Fully mixed buffer tank.

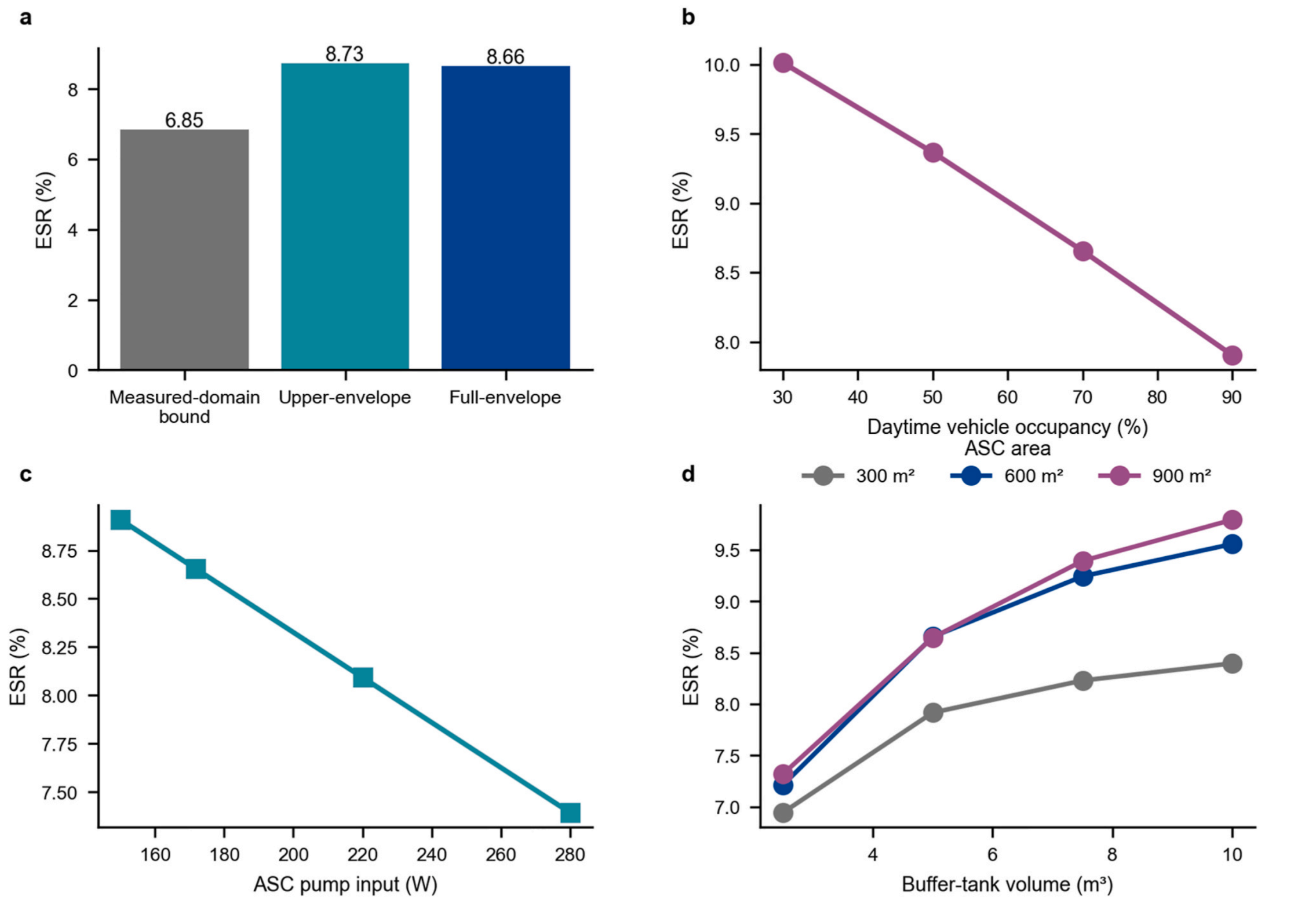

Fig. 12. Sensitivity analysis: (a) heat-pump map treatment, (b) daytime vehicle occupancy, (c) ASC pump input, and (d) buffer-tank volume at three ASC areas.

Tank stratification is a model-form uncertainty. Because no stratified-tank model or measured temperature profile is available, the analysis does not add an assumed 1–3 percentage-point benefit to the base result.

Collector area, tank volume, pipe burial depth, pipe spacing, and control strategy are reported as controllable design variables. Parking occupancy, irradiance bias, pavement properties, demand, and model-form discrepancy are reported separately as uncertain inputs.

Heat-pump uncertainty is represented by alternative map-boundary treatments because the manufacturer-map model contains no fitted second-law-efficiency parameter. The separate effects of building and vehicle shading on annual ASC heat yield and ESR are shown in Fig. 13.

Annual Method A ESR ranges from 7.41% to 9.73% over 2015–2024, with a mean of 8.66% and a sample standard deviation of 0.72 percentage points. Annual heat yield ranges from 21.80 to 26.32 kWh m^{-2} yr^{-1} (see Fig. 14).

Uncertainty is reported through transparent scenario ranges because probability distributions are not available for site occupancy or pavement model discrepancy. Manufacturer-map treatments and uncertain inputs are kept separate from controllable design variables.

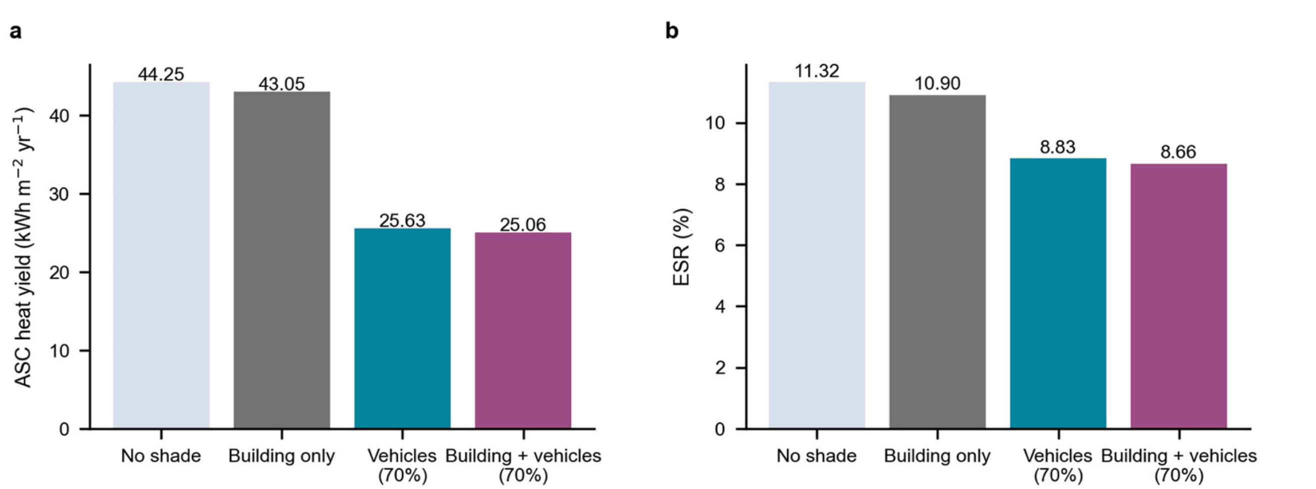

Fig. 13. Attribution of (a) annual ASC heat yield and (b) ESR to building and vehicle shading. Vehicle occupancy is 70% during business hours in the reference scenario.

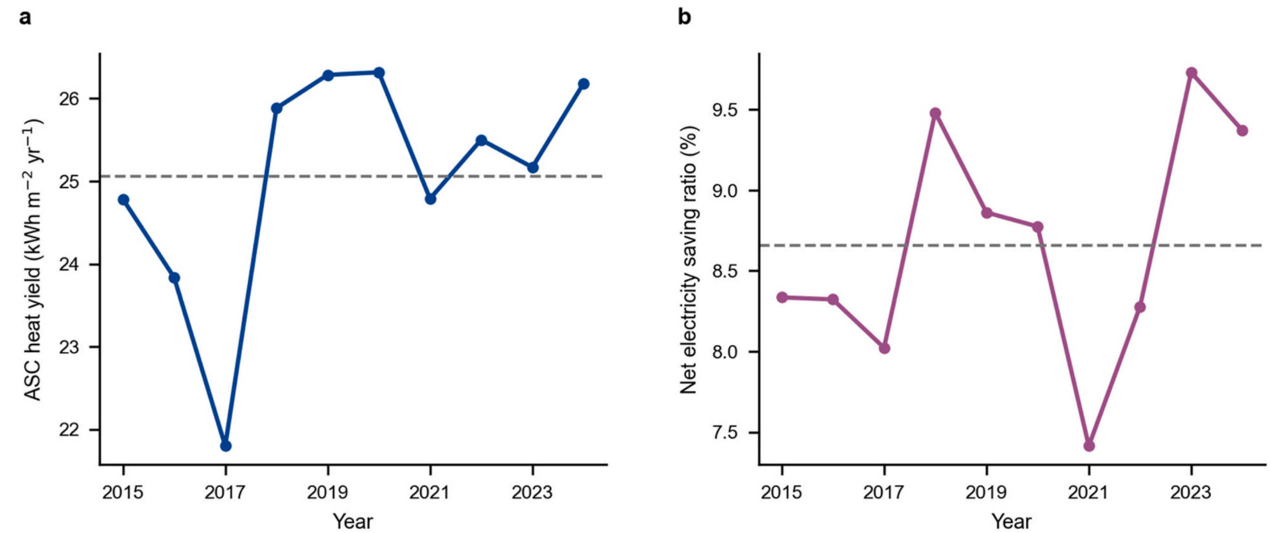

Fig. 14. Interannual variability (2015–2024): annual ASC heat yield and annual electricity-saving ratio. The coefficient of variation of ESR is 8.35%.

Because reliable probability distributions were unavailable for several uncertain inputs, uncertainty was evaluated using scenario-based ranges rather than Monte Carlo simulation. The resulting ESR ranges were 7.90–10.01% for vehicle occupancy, 6.85–8.73% for heat-pump map treatment, and 7.39–8.91% for pump selection. The resulting ranges for uncertain inputs and controllable design variables are summarised in Fig. 15.

3.5. Design optimisation

Across the 300–900 m^2 area and 2.5–10 m^3 storage grid, ESR ranges from 6.94% to 9.80%, as shown in Fig. 16. At 5 m^3, increasing area beyond 750 m^2 does not improve ESR because additional collection increasingly coincides with the upper boundary of the measured heat-pump map.

The grid is interpreted as a bounded design sensitivity. Midpoint capital costs scale the collector installation with area and the ASC-specific tank with storage volume.

Within the tested domain, the largest ESR is 9.80% at 900 m^2/10 m^3, compared with 8.66% for the 600 m^2/5 m^3 reference design. The small absolute gain does not support increasing collector area solely to reduce heat-pump electricity.

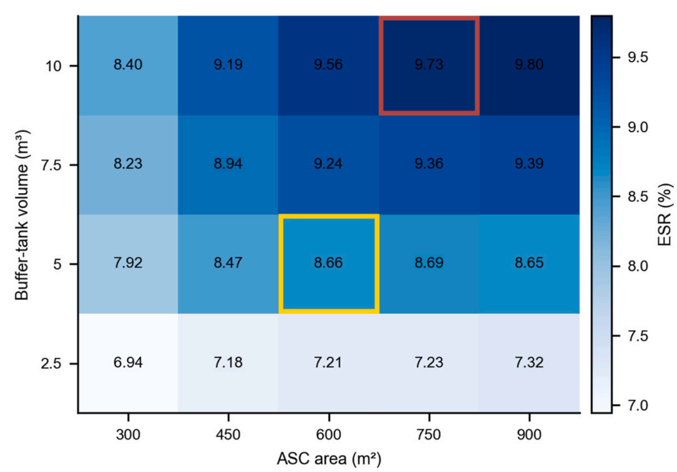

Fig. 16. Ten-year mean ESR for Method A over the ASC-area × buffer-volume grid. The star marks the 600 m^2/5 m^3 reference and the red outline marks the highest ESR.

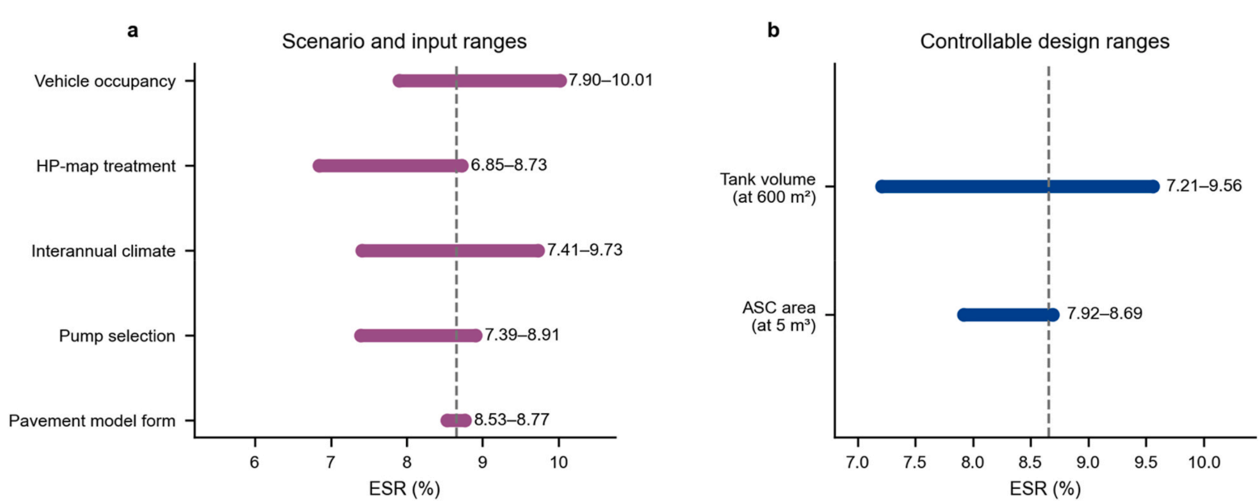

Fig. 15. ESR ranges obtained by varying (a) scenario-based uncertain inputs and (b) controllable design variables. The dashed line indicates the reference-case ESR of 8.66%.

Because all tested configurations remain economically unfavourable on electricity savings alone, the ESR-cost trade-off shown in Fig. 17 does not identify a cost-performance knee as an economically optimal design.

3.6. Economic assessment

The economic performance of the ASC–HP system was evaluated using traceable cost data from published sources and official statistics.

(1) Electricity price.

The Lithuanian household electricity price was €0.23 kWh^{-1} in the second half of 2024 [45]. A similar residential price including taxes, €0.239 kWh^{-1}, was reported for September 2025 [46]. A reference value of €0.23 kWh^{-1} was therefore adopted.

(2) ASC installation cost.

The marginal cost of embedding pipes in asphalt pavement varies widely with project type and local construction conditions. Reported values range from approximately €23 m^{-2} for the piping addition alone in new construction [47] to about €115 m^{-2} for adding solar collection during road resurfacing [48]. To reflect uncertainty between new-build and retrofit scenarios, a range of €25–80 m^{-2} was adopted for ASC pipe installation.

(3) Heat pump cost.

Water-to-water heat pumps in the 10–30 kW range typically cost €12,000–18,000 for the unit, plus €2000–3000 for installation [49]. Because the heat pump is required in the baseline system regardless of ASC integration, only the incremental cost of ASC-related components is considered here.

Table 5 summarises the estimated incremental investment associated with the ASC upgrade relative to a baseline heat pump system.

Under Method A, annual electricity use falls from 8515 to 7778 kWh yr^{-1}, a saving of approximately 737 kWh yr^{-1}. At €0.23 kWh^{-1}, the annual monetary saving is approximately €170 yr^{-1}. The corresponding simple payback is approximately 128–366 years for the €21,750–62,000 incremental-cost range (see Fig. 18).

Even the lower-bound payback is far longer than the assumed 25-year service life. The ASC upgrade is therefore not viable on electricity savings alone under the stated prices and requires a separately demonstrated non-energy value proposition.

The levelised cost of saved electricity (LCOSE) can be estimated as:

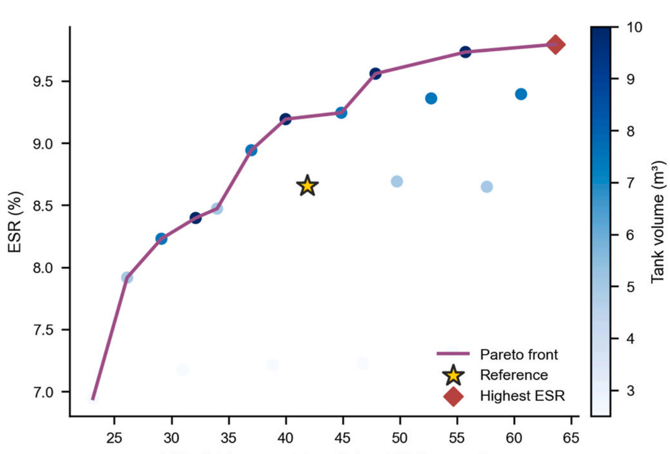

Fig. 17. ESR versus midpoint incremental capital cost for the area–storage grid. The Pareto front, 600 m^2/5 m^3 reference, and highest-ESR design are identified.

Table 5
Estimated incremental investment cost of the ASC upgrade relative to a baseline heat pump system.

Cost component	Low estimate	High estimate	Unit	Source
ASC pipe installation (600 m^2)	15,000	48,000	€	€25–80 m^{-2}
Buffer tank (5 m^3, insulated)	4000	8000	€	Market survey
Transport piping (25 m, pre-insulated)	1250	2500	€	EN ISO 15698
Circulation pump + controls	1500	3500	€	Market survey
Total incremental investment	21,750	62,000	€	

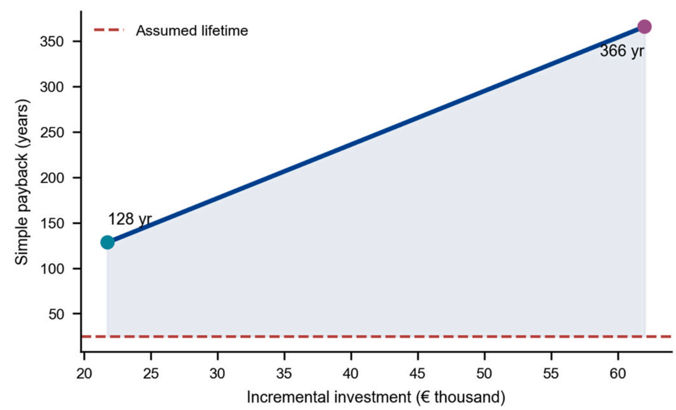

Fig. 18. Simple payback as a function of incremental investment using the annual electricity saving of 737 kWh yr^{-1} and an electricity price of €0.23 kWh^{-1}. The dashed line denotes the assumed 25-year service life.

$$\text{LCOSE} = \frac{\text{Total investment}}{\text{Annual electricity saving} \times \text{System lifetime}} \tag{26}$$

Without discounting, dividing incremental cost by 25 years of electricity savings gives an LCOSE of approximately €1.18–3.36 kWh^{-1}, well above the adopted retail electricity price. Discounting would increase these values further.

The area–storage sensitivity does not overturn this finding: increasing tank volume from 5 to 10 m^3 raises ESR by less than one percentage point at 600 m^2. The 600 m^2/5 m^3 case is therefore retained as the site-constrained reference, not claimed as an economic optimum.

3.7. Life-cycle carbon assessment

At a grid intensity of 0.16 kg CO_2 kWh^{-1}, operational emissions are 1.362 t CO_2 yr^{-1} for the no-ASC heat-pump baseline and 1.245 t CO_2 yr^{-1} for Method A. The incremental ASC therefore avoids approximately 0.118 t CO_2 yr^{-1}, or 8.66%, relative to the consistent heat-pump baseline. The much larger reduction relative to CHP district heating is primarily attributable to heat-pump electrification and is not assigned to the ASC subsystem.

The functional service is 1 MWh of DHW delivered at 50 °C. The incremental system boundary contains the ASC pipework, transport loop, circulation pump and controls, working fluid, and the ASC-specific 5 m^3 low-temperature buffer tank.

The existing OpenLCA inventory quantifies only the collector-loop portion of this incremental boundary and reports 272 kg CO_2-eq m^{-2}, or approximately 163 t CO_2-eq for 600 m^2. Because the buffer tank was omitted from that inventory, the value is retained only as a lower-bound screening burden and is not presented as a complete comparative LCA result. The resulting partial cradle-to-use inventory for the collector loop is summarised in Table 6.

Purchasing power parity (PPP) was used to transfer the UK baseline ([50]) cost data to the target context. Unlike a market exchange rate, a PPP conversion factor acts as a spatial price deflator, controlling for differences in the domestic purchasing power of currencies across economies. The UK-derived material, transport and labour costs were therefore adjusted by multiplying each baseline value by the ratio of the target-economy PPP factor to the UK factor, using World Bank International Comparison Program data for the same reference year [51].

The lower-bound collector-loop burden of approximately 163 t CO_2-eq already exceeds the 25-year incremental operational saving of approximately 2.95 t CO_2 under the current grid. Accordingly, no carbon payback occurs within the assumed service life. Grid decarbonisation further reduces the avoided operational emissions per kilowatt-hour.

3.8. Comparison with previous studies and alternative systems

The simulated specific yield is 25.06 kWh m^{-2} yr^{-1}, below dedicated direct-heating ASC installations because this system operates against a seasonally warm buffer-tank return and is additionally constrained by building and vehicle shading. Heat-pump SCOP increases from 3.58 to 4.01, while system SPF is 3.92 after ASC pumping is included.

Table 7 compares systems supplying the same 30.5 MWh yr^{-1} DHW service. The comparison separates the performance of the complete heat-pump system from the incremental contribution of the ASC and should not be interpreted as attributing the full heat-pump advantage to ASC.

The ASC-assisted system has an SPF of 3.92 and uses 7.78 MWh yr^{-1}, compared with 8.52 MWh yr^{-1} for the same heat pump without ASC. The principal advantage of the ASC-assisted system is that it uses existing pavement area without competing for rooftop space. However, under the assumptions adopted in this study, the additional energy savings and the associated economic and carbon benefits provided by the ASC subsystem are limited.

Table 6
Partial cradle-to-use inventory for the collector loop. The table is a lower-bound screening result because the incremental ASC-specific buffer tank is not represented.

Life-cycle stage (EN 15804)	Flow	Reference quantity (1 m^2 collector)	Unit cost, subarctic supply chain (€ m^{-2})
A1–A3 Production	Bitumen binder	5.6 kg	4.32
A1–A3 Production	PEX pipe (Ø24 mm, 0.20 m spacing → 5.0 m m^{-2})	5.0 m	22.44
A1–A3 Production	Ethylene glycol (working fluid)	0.21 kg	0.12
A1–A3 Production	Deionised water	0.50 kg	0.10
A4 Transport	Freight transport of materials	3.25 t km	0.23
A5 Installation	Construction diesel	0.17 L	0.29
A5 Installation	On-site labour	0.20 h	7.83
B6 Use (25 yr)	Circulation-pump electricity	7.09 kWh	1.63
Total	Unit cost	—	36.96
Impact results (cradle-to-use)	GWP 272 kg CO_2-eq m^{-2}; AP 1.57 kg SO_2-eq m^{-2}	—	—
Excluded	ASC-specific buffer tank not represented; pavement reconstruction, routine maintenance, end-of-life modules C1–C4 and D	—	—

3.9. Design guidelines, transferability and limitations

Based on the present simulations and sensitivity analyses, the following preliminary design indications apply to systems with comparable DHW demand, pavement geometry, and high-latitude operating conditions.

First, an ASC area of approximately 20–40 m^2 per 1000 kWh yr^{-1} of DHW demand appears to provide a reasonable balance between performance and cost-effectiveness.

Second, a buffer tank volume of 8–15 L per m^2 of ASC area is recommended. Below 5 L m^{-2}, the tank tends to saturate frequently and reject potentially useful heat, whereas above 20 L m^{-2} the incremental benefit becomes negligible.

Third, fixed-flow control with differential-temperature on/off switching is recommended for systems with ASC areas below 1000 m^2. For this scale, the added cost and complexity of variable-flow control are not justified by the marginal, or even negative, improvement in ESR.

Fourth, the baseline pipe burial depth of 50 mm provides a reasonable compromise between thermal performance and structural protection. Deeper installation, in the range of 80–100 mm, increases thermal resistance by approximately 30–50% but may improve long-term durability.

Finally, at 55°N, meaningful ASC operation is limited to approximately April through October. System design and economic evaluation should therefore be based on an effective seven-month operation period rather than a full-year solar contribution.

These recommendations are derived from a single case study and should be further validated for other sites, building types, and climatic conditions.

The following limitations bound the results. First, the heat-pump map contains six manufacturer test points. Edge trends are extended only within the published −10 to 30 °C source-water operating range, and the measured-domain boundary case is reported separately. Second, the quasi-steady pavement and fully mixed tank representations introduce model-form uncertainty that is not equivalent to experimental validation. Third, parking occupancy is scenario-based rather than measured on site, although the full polygon-shadow sensitivity is reported. Fourth, the integrated ASC–heat-pump system has not been experimentally validated. Finally, the incremental economic and life-cycle boundaries include the ASC-specific low-temperature tank consistently.

4. Conclusion

This study evaluated seasonal source-side preheating from an asphalt solar collector coupled to a water-source heat pump for DHW in Kaunas, Lithuania (54.9°N). The ten-year hourly simulation uses polygon-union shading, flow-regime-specific hydraulics, and a capacity-matched manufacturer heat-pump map. The main conclusions are:

Under fixed-flow control, the 600 m^2 ASC delivers 25.06 kWh m^{-2} yr^{-1}. It increases heat-pump SCOP from 3.58 to 4.01; after ASC pumping is included, system SPF is 3.92 and net ESR is 8.66%. These figures describe seasonal source-side preheating, not year-round source replacement.

Variable-flow control increases gross collection by approximately 4.6–4.7% but lowers ESR to 6.60–7.04%. Fixed-flow control therefore remains preferable for the studied configuration.

Within the tested design domain, increasing tank volume provides more benefit than increasing collector area. The maximum ESR is 9.80% at 900 m^2/10 m^3; the original 600 m^2/5 m^3 design provides 8.66%, while occupancy scenarios span 7.90–10.01%.

Overlapping shadows, limited solar access during winter, hydraulic auxiliaries, and the constrained heat-pump operating range significantly limit the potential system benefits. Given Kaunas's specific climatic, spatial, and economic factors, the ASC subsystem probably is unlikely to support large-scale use if its primary justification is solely based on DHW

Table 7
Quantitative comparison under a unified service boundary (30.5 MWh yr^{-1} DHW, Kaunas). ASC–HP values from this study; other systems are engineering estimates under the assumptions stated in the text.

System	SPF_{sys} or annual-mean η_{th}	Electricity (MWh yr^{-1})	Operational CO_2 (t yr^{-1})	Specific yield (kWh m^{-2} yr^{-1})	Basis
ASC–HP (600 m^2 lot, this study)	SPF_{sys} = 3.92 (HP SCOP = 4.01)	7.78	1.24	25.06	Ten-year simulation (this work)
GSHP, closed-loop borehole	SPF 3.8–4.5	6.8–8.0	1.1–1.3	n/a	Field-trial range [52]
ASHP, cold-climate	SPF 2.4–3.0	10.2–12.7	1.6–2.0	n/a	Field-trial range [52]
Flat-plate solar thermal (30 m^2, 45° S)	η_{th} 0.38–0.42	pump only	≈0 (collector loop)	450–500	Backup heat source required; η from [53]
Evacuated-tube solar thermal (30 m^2)	η_{th} 0.48–0.53	pump only	≈0 (collector loop)	565–625	Backup heat source required; η from [53]
Liquid PVT (30 m^2)	η_{th} 0.28–0.35 (+electricity)	depends on coupling	low	330–410 (thermal side)	Estimate [16]

electricity savings or reducing operational carbon emissions.

Future applications should target locations with high annual solar irradiance, little shading from structures and vehicles, and extensive open pavement areas. The concept becomes more attractive when collector pipes can be installed cost-effectively during new pavement construction or resurfacing, or when additional benefits like pavement cooling or seasonal heat storage are demonstrated. These findings primarily define the deployment limits of ASC-assisted heat pumps in high-latitude urban environments rather than prescribe exact implementation.

CRediT authorship contribution statement

Lianghan Cong: Writing – original draft, Formal analysis, Data curation, Conceptualization. **Shuaiyi Lu:** Writing – review & editing, Formal analysis, Data curation. **Pan Jiang:** Writing – review & editing. **Lan Liu:** Formal analysis. **Xiaoshu Lü:** Writing – review & editing, Supervision, Funding acquisition.

Declaration of generative AI and AI-assisted technologies in the writing process

During the preparation of this work, the authors utilised Codex to improve the English language presentation. After employing this service, the authors carefully reviewed and edited the content as necessary, and they take full responsibility for the content of the published article.

Declaration of competing interest

The authors declare the following financial interests/personal relationships which may be considered as potential competing interests: Xiaoshu Lu reports financial support was provided by European Commission. If there are other authors, they declare that they have no known competing financial interests or personal relationships that could have appeared to influence the work reported in this paper.

Acknowledgments

This work was supported by the European Union for the projects EnhanceEurope (27000654121).

Appendix A. Supplementary data

Supplementary data to this article can be found online at https://doi.org/10.1016/j.energy.2026.142243.

Data availability

All meteorological and radiation data used in this study are publicly available from the ERA5 reanalysis dataset through the Copernicus Climate Data Store (https://cds.climate.copernicus.eu/). The DHW demand profile was derived from measured district-heating substation records for the B92 building collected from May 2018 to September 2021; its processing and use are described in Section 3.1 and Supplementary Section S5. The governing equations, model parameters, boundary conditions, control logic, and computational workflow required to reproduce the simulations are provided in Section 2, Appendices A1–A3, and Supplementary Table S1–S4.

References

[1] IEA. Tracking clean energy progress 2023. Paris: International Energy Agency; 2023.
[2] European Commission. EU building stock observatory. 2020.
[3] Energy consumption in households n.d. https://ec.europa.eu/eurostat/statistics-explained/index.php?title=Energy_consumption_in_households (accessed March 10, 2026).
[4] Soleimani A, Davidsson P, Malekian R, Spalazzese R. Modeling hybrid energy systems integrating heat pumps and district heating: a systematic review. Energy Build 2025;329:115253. https://doi.org/10.1016/j.enbuild.2024.115253.
[5] Zhu M, Pergantis EN, Kim J, Dai C, James N, Oh J, et al. A critical review of electrochemical heat pump technologies: status, challenges, and perspectives. Appl Therm Eng 2026;286:129232. https://doi.org/10.1016/j.applthermaleng.2025.129232.
[6] Wu J, Sun S, Song Q, Sun D, Wang D, Li J. Energy, exergy, exergoeconomic and environmental (4E) analysis of cascade heat pump, recuperative heat pump and carbon dioxide heat pump with different temperature lifts. Renew Energy 2023;207:407–21. https://doi.org/10.1016/j.renene.2023.03.028.
[7] Wen S, Shen B, Yao Y, Chen Q. Energy performance and life-cycle analyses of advanced terminal devices and heat pumps for a medium-sized office building in different climate zones in China. Energy Build 2025;342:115835. https://doi.org/10.1016/j.enbuild.2025.115835.
[8] Arpagaus C, Bless F, Uhlmann M, Schiffmann J, Bertsch SS. High temperature heat pumps: market overview, state of the art, research status, refrigerants, and application potentials. Energy 2018;152:985–1010. https://doi.org/10.1016/j.energy.2018.03.166.
[9] Staffell I, Brett D, Brandon N, Hawkes A. A review of domestic heat pumps. Energy Environ Sci 2012;5:9291–306. https://doi.org/10.1039/C2EE22653G.
[10] Aridi M, Pannier M-L, Aridi R, Lemenand T. A comprehensive review of life cycle assessments for domestic heat pumps: environmental footprint and future directions. Energy Build 2025;336:115605. https://doi.org/10.1016/j.enbuild.2025.115605.
[11] Namdar H, Rossi di Schio E, Semprini G, Valdiserri P. Photovoltaic-thermal solar-assisted heat pump systems for building applications: a technical review on direct expansion systems. Energy Build 2025;334:115516. https://doi.org/10.1016/j.enbuild.2025.115516.
[12] Fadzlin WA, Hasanuzzaman M, Rahman SA, Said Z. Solar thermal energy storage: global challenges, innovations, and future directions for renewable energy systems. Appl Therm Eng 2025;280:128346. https://doi.org/10.1016/j.applthermaleng.2025.128346.
[13] Zou L, Liu Y, Yu M, Yu J. A review of solar assisted heat pump technology for drying applications. Energy 2023;283:129215. https://doi.org/10.1016/j.energy.2023.129215.
[14] Alsarraf J, Alnaqi AA, Al-Rashed AAAA. Comparative thermo-environ-economic analysis of solar-assisted and conventional ejector-compression heat pump systems for space heating. Energy Build 2026;354:116952. https://doi.org/10.1016/j.enbuild.2026.116952.
[15] Sezen K, Gungor A. Comparison of solar assisted heat pump systems for heating residences: a review. Sol Energy 2023;249:424–45. https://doi.org/10.1016/j.solener.2022.11.051.
[16] Herrando M, Wang K, Huang G, Otanicar T, Mousa OB, Agathokleous RA, et al. A review of solar hybrid photovoltaic-thermal (PV-T) collectors and systems. Prog

Energy Combust Sci 2023;97:101072. https://doi.org/10.1016/j.pecs.2023.101072.
[17] Lv D, Ran D, Yang Q, Zhang W, Zhao Y, Liu G, et al. Performance analysis and city applicability evaluation of a transcritical CO2 heat pump system integrated with expander-compressor unit subcooling for space heating. Energy 2025;320:135293. https://doi.org/10.1016/j.energy.2025.135293.
[18] Gong Y, Ma G, Song Y, Wang L, Nie J, Wang L. Performance study of ultra-low temperature district heating system based on double-loop booster heat pump control strategy. Appl Therm Eng 2025;269:126084. https://doi.org/10.1016/j.applthermaleng.2025.126084.
[19] Xin X, Liu Y, Zhang Z, Zheng H, Zhou Y. A day-ahead operational regulation method for solar district heating systems based on model predictive control. Appl Energy 2025;377:124619. https://doi.org/10.1016/j.apenergy.2024.124619.
[20] Fischer D, Madani H. On heat pumps in smart grids: a review. Renew Sustain Energy Rev 2017;70:342–57. https://doi.org/10.1016/j.rser.2016.11.182.
[21] Talha T, Talha M, Liu S, Mazhar AR, Perwez U, Moiz M, et al. Experimental study of unglazed transpired solar collectors integrated with buildings in humid subtropics. Energy Build 2025;339:115767. https://doi.org/10.1016/j.enbuild.2025.115767.
[22] Bobes-Jesus V, Pascual-Muñoz P, Castro-Fresno D, Rodriguez-Hernandez J. Asphalt solar collectors: a literature review. Appl Energy 2013;102:962–70. https://doi.org/10.1016/j.apenergy.2012.08.050.
[23] Abbas FA, Alhamdo MH. Numerical modeling and experimental validation of an asphalt solar collector using fins. Sol Energy 2024;273:112529. https://doi.org/10.1016/j.solener.2024.112529.
[24] Buscemi A, Beccali M, Guarino S, Lo Brano V. Coupling a road solar thermal collector and borehole thermal energy storage for building heating: first experimental and numerical results. Energy Convers Manag 2023;291:117279.
[25] Pasetto M, Baliello A, Giacomello G, Pasquini E. Optimisation of a road asphalt solar collector for energy harvesting. Road Mater Pavement Des 2025;26:72–90. https://doi.org/10.1080/14680629.2025.2489031.
[26] Guldentops G, Nejad AM, Vuye C, Van den bergh W, Rahbar N. Performance of a pavement solar energy collector: model development and validation. Appl Energy 2016;163:180–9. https://doi.org/10.1016/j.apenergy.2015.11.010.
[27] Ghalandari T, Maleki A, Golmohammadi A, Verhaert I, Vuye C. Thermal and economic analysis of asphalt solar collectors using a field-scale experimental setup. Appl Therm Eng 2026;287:129426. https://doi.org/10.1016/j.applthermaleng.2025.129426.
[28] Amara WB, Jannouf A, Bouabidi A, Rashid FL, Kadhim SA, Chrigui M, et al. Evaluation of heat transfer and thermal efficiency in asphalt solar collector: numerical model validation and pipe design effects. Appl Therm Eng 2025;278:127569. https://doi.org/10.1016/j.applthermaleng.2025.127569.
[29] Nettestroth J, Rosebrock O, Kupšys K, Mačiulis V, Rovbutas I. Solar energy for multi family houses in Lithuania: potential implementation. Berlin, Germany: Initiative Wohnungswirtschaft Osteuropa e.V. (IWO); 2019.
[30] Huld T, Mueller R, Gambardella A. A new solar radiation database for estimating PV performance in Europe and Africa. Sol Energy 2012;86:1803–15. https://doi.org/10.1016/j.solener.2012.03.006.
[31] Spencer JW. Fourier series representation of the position of the sun, vol. 2. Search; 1971172+.
[32] Report - Vehicles in use. Europe 2023. ACEA - European automobile manufacturers' association 2023. https://www.acea.auto/publication/report-vehicles-in-use-europe-2023/. [Accessed 11 April 2026].
[33] Parking generation manual. Institute of Transportation Engineers; 2019.
[34] Bergman TL, Lavine AS, Incropera FP, DeWitt DP. Fundamentals of heat and mass transfer. John Wiley & Sons; 2020.
[35] Bergman TL, Lavine AS, Incropera FP, DeWitt DP. Fundamentals of heat and mass transfer. eighth ed. Hoboken, NJ: Wiley; 2018.
[36] Florschuetz LW. Extension of the Hottel-Whillier model to the analysis of combined photovoltaic/thermal flat plate collectors. Sol Energy 1979;22:361–6. https://doi.org/10.1016/0038-092X(79)90190-7.
[37] Solaimanian M, Kennedy TW. Predicting maximum pavement surface temperature. Transp Res Rec 1993;1417:1–11.
[38] Morkunaite L, Pupeikis D, Tsalikidis N, Ivaskevicius M, Manhanga FC, Cerneckiene J, et al. Efficiency in building energy use: pattern discovery and crisis identification in hot-water consumption data. Energy Build 2025;336:115579. https://doi.org/10.1016/j.enbuild.2025.115579.
[39] Kusuda T, Achenbach PR. Earth temperature and thermal diffusivity at selected stations in the United States. Washington, DC: National Bureau of Standards; 1965. https://doi.org/10.6028/NBS.RPT.8972.
[40] Hasrat IR, Jensen PG, Larsen KG, Srba J. Modelling of hot water buffer tank and mixing loop for an intelligent heat pump control. In: Cimatti A, Titolo L, editors. Formal methods for industrial critical systems. Cham: Springer Nature Switzerland; 2023. p. 113–30. https://doi.org/10.1007/978-3-031-43681-9_7.
[41] Soares A, Camargo J, Al-Koussa J, Diriken J, Van Bael J, Lago J. Efficient temperature estimation for thermally stratified storage tanks with buoyancy and mixing effects. J Energy Storage 2022;50:104488. https://doi.org/10.1016/j.est.2022.104488.
[42] Johnsson J, Adl-Zarrabi B. A numerical and experimental study of a pavement solar collector for the northern hemisphere. Appl Energy 2020;260:114286. https://doi.org/10.1016/j.apenergy.2019.114286.
[43] Buscemi A, Guarino S, Biondi A, Beccali M, Lo Brano V. Design optimization of road thermal collectors: a numerical and experimental study in the mediterranean. Energy 2025;333:137473. https://doi.org/10.1016/j.energy.2025.137473.
[44] Ghalandari T, Baetens R, Verhaert I, Snm Nasir D, Van den bergh W, Vuye C. Thermal performance of a controllable pavement solar collector prototype with configuration flexibility. Appl Energy 2022;313:118908. https://doi.org/10.1016/j.apenergy.2022.118908.
[45] Eurostat. Electricity prices for household consumers. 2024.
[46] GlobalPetrolPrices.com. Lithuania electricity prices. 2025. September 2025.
[47] Ao K, Sa W. Exploring the potentials of asphalt solar collectors in hot humid climates. Innovative Energy & Research 2016;5(141):2.
[48] Asphalt solar collector renewable heat for IHT | solar collectors | solar recharge for GSHP | pavement solar collectors | Road Solar Thermal Collector n.d. https://www.icax.co.uk/asphalt_solar_collector.html (accessed January 10, 2026).
[49] autarc.energy. Heat pump costs 2025: Water-to-water heat pump. 2025.
[50] Studios L. Asphalt collector. Cyclifier n.d. https://www.cyclifier.org/project/asphalt-collector/(accessed January 10, 2026).
[51] World Bank. PPP conversion factor, GDP (LCU per international $). World Development Indicators, International Comparison Program. 2015. Indicator PA.NUS.PPP.
[52] Gleeson CP, Lowe R. Meta-analysis of European heat pump field trial efficiencies. Energy Build 2013;66:637–47. https://doi.org/10.1016/j.enbuild.2013.07.064.
[53] Maraj A, Londo A, Firat C, Gebremedhin A. Comparison of the energy performance between flat-plate and heat pipe evacuated tube collectors for solar water heating systems under mediterranean climate conditions. J Sustain Dev Energy Water Environ Syst 2019;7:87–100. https://doi.org/10.13044/j.sdewes.d6.0228.